Twisted bilayer graphene. II. Stable symmetry anomaly

Zhi-Da Song , ¹ Biao Lian, ¹ Nicolas Regnault, ^{1,2} and B. Andrei Bernevig ^{1,*}

¹Department of Physics, Princeton University, Princeton, New Jersey 08544, USA

²Laboratoire de Physique de l'Ecole Normale Superieure, ENS, Université PSL, Centre National de la Recherche Scientifique, Sorbonne Université, Université Paris-Diderot, Sorbonne Paris Cité, Paris 75005, France



(Received 28 October 2020; revised 15 April 2021; accepted 16 April 2021; published 11 May 2021)

We show that the entire continuous model of twisted bilayer graphene (TBG) (and not just the two active bands) with particle-hole symmetry is anomalous and hence incompatible with lattice models. Previous works [e.g., Z. Song, Z. Wang, W. Shi, G. Li, C. Fang, and B. A. Bernevig, Phys. Rev. Lett. 123, 036401 (2019); J. Ahn, S. Park, and B.-J. Yang, Phys. Rev. X 9, 021013 (2019); H. C. Po, L. Zou, T. Senthil, and A. Vishwanath, Phys. Rev. B 99, 195455 (2019); J. Kang and O. Vafek, Phys. Rev. X 8, 031088 (2018); M. Koshino, N. F. Q. Yuan, T. Koretsune, M. Ochi, K. Kuroki, and L. Fu, Phys. Rev. X 8, 031087 (2018); J. Liu, J. Liu, and X. Dai, Phys. Rev. B 99, 155415 (2019); L. Zou, H. C. Po, A. Vishwanath, and T. Senthil, Phys. Rev. B 98, 085435 (2018)] found that the two flatbands in TBG possess a fragile topology protected by the $C_{2z}T$ symmetry. Song et al. [Z. Song, Z. Wang, W. Shi, G. Li, C. Fang, and B. A. Bernevig, Phys. Rev. Lett. 123, 036401 (2019)] also pointed out an approximate particle-hole symmetry (P) in the continuous model of TBG. In this paper, we numerically confirm that \mathcal{P} is indeed a good approximation for TBG and show that the fragile topology of the two flatbands is enhanced to a \mathcal{P} -protected stable topology. This stable topology implies 4l + 2 ($l \in \mathbb{N}$) Dirac points between the middle two bands. The \mathcal{P} -protected stable topology is robust against arbitrary gap closings between the middle two bands and the other bands. We further show that, remarkably, this \mathcal{P} -protected stable topology, as well as the corresponding 4l + 2 Dirac points, cannot be realized in lattice models that preserve both $C_{2z}T$ and \mathcal{P} symmetries. In other words, the continuous model of TBG is anomalous and cannot be realized on lattices. Two other topology related topics, with consequences for the interacting TBG problem, i.e., the choice of Chern band basis in the two flatbands and the perfect metal phase of TBG in the so-called second chiral limit, are also discussed.

DOI: 10.1103/PhysRevB.103.205412

I. INTRODUCTION

Twisted bilayer graphene (TBG) at the first magic angle ($\theta \approx 1.05^{\circ}$) exhibits a group of two almost exactly flat bands [1]. Due to the interesting interaction of insulating and conducting states [2-32], superconductor states [33-51], and single-particle topology [19,52–65] in the flatbands, TBG represents one of the most versatile physical systems of recent years [1-31,33-63,65-113]. References [54,56] showed that the $C_{2z}T$ symmetry of TBG protects a fragile topology [80,114–118] of the two flatbands, which is characterized by a \mathbb{Z} -valued winding number. The fragile topology manifests itself as a topological obstruction for exponentially decaying Wannier functions satisfying $C_{2z}T$ symmetry for the two flatbands. However, the Wannier obstruction can be removed by adding trivial bands into the consideration [80,114,115]. For example, Ref. [55] showed explicitly that symmetric Wannier functions can be constructed if certain additional orbitals are coupled to the fragile topological band protected by $C_{2z}T$. However, the papers arguing for a trivialization of the bands [54,55] neglected one (approximate) symmetry of the TBG model [1].

The Bistritzer-MacDonald (BM) model [1] of TBG has an approximate particle-hole symmetry \mathcal{P} first pointed out in Ref. [56]. It was already pointed out in Ref. [56] that with this approximate symmetry there seems to be a further, stable topology in TBG, but this result was not further expanded. We here numerically confirm that the error—on the wave functions—of the \mathcal{P} symmetry (defined in Sec. II B) in the BM model of TBG is extremely small (<0.01). Thus we count \mathcal{P} symmetry as a good approximation for the lowenergy physics in TBG. We prove that if the $C_{2z}T$ protected winding number of the two flatbands is odd (true in TBG) then the two flatbands have a stable topology protected by \mathcal{P} , which is characterized by a \mathbb{Z}_2 invariant δ . In contrast to the fragile topological bands, which can be trivialized by being coupled to certain trivial bands, the \mathbb{Z}_2 topology, as well as the Wannier obstruction implied by the \mathbb{Z}_2 invariant, is stable against adding trivial bands that preserve the \mathcal{P} symmetry. We further proved that, in the presence of $C_{2z}T$ and \mathcal{P} , the \mathbb{Z}_2 invariant δ of 2M particle-hole symmetric bands $\epsilon_{-M}(\mathbf{k})\cdots\epsilon_{-1}(\mathbf{k}), \epsilon_{1}(\mathbf{k})\cdots\epsilon_{M}(\mathbf{k})$ is related to the number of Dirac points N_D between $\epsilon_{-1}(\mathbf{k})$ and $\epsilon_1(\mathbf{k})$ in the first Brillouin zone (BZ) as $\delta = \frac{N_D}{2} \mod 2$, provided that the 2M bands are gapped from higher and lower bands. Here $\epsilon_n(\mathbf{k})$ [$\epsilon_{-n}(\mathbf{k})$] is the *n*th positive (negative) band. Therefore, as long as 4l + 2 $(l \in \mathbb{N})$ Dirac points exist between $\epsilon_{-1}(\mathbf{k})$ and $\epsilon_{1}(\mathbf{k})$ we find that 2M, $\forall M \in \mathbb{N}$ particle-hole symmetric bands (separate in

^{*}bernevig@princeton.edu

energy from the M+1, M+2... and ..., -M-2, -M-1bands) have $\delta = 1$ and hence are topologically nontrivial. The feature of TBG that arbitrary 2M bands are topological is inconsistent with lattice models with $C_{2z}T$ and \mathcal{P} symmetry. In a lattice model, if 2M is large enough, e.g., equals to the number of orbitals in the model, the 2M bands have to be topologically trivial because they span the Hilbert space of the local orbitals. Therefore, the \mathbb{Z}_2 topology, and the 4l+2Dirac points accordingly, cannot be realized in lattice models with finite number of orbitals. We hence call the \mathbb{Z}_2 topology an anomaly of the $C_{2z}T$ and ${\mathcal P}$ symmetries. We further note that this implies that the many-body U(4) and $U(4) \times U(4)$ symmetries [110–112] are incompatible with a lattice model and hence anomalous. It also implies that the lattice models built to model TBG [19,52,53,55] have to break the \mathcal{P} symmetry or the $C_{2z}T$ symmetry of the TBG model.

This paper is organized as follows. In Sec. II, we present a review of the BM model of TBG and summarize its symmetries. The error of the approximate particle-hole symmetry \mathcal{P} is defined and is confirmed as being small (<0.01). In Sec. III, we prove that the \mathcal{P} symmetry protects a stable \mathbb{Z}_2 topological state. In Sec. IV, a no-go theorem of the \mathbb{Z}_2 topology is proved for lattice models with the $C_{2z}T$ and \mathcal{P} symmetries. The relation between the \mathbb{Z}_2 invariant and the number of Dirac points is also established in this section. In Sec. V, we show that, when the two flatbands are gapped from the other bands, there is a natural choice of Chern band basis (with opposite Chern numbers) in the two flatbands. The Chern band basis is used in our interacting works [110–113] on TBG. In Sec. VI, we show that, in the so-called second chiral limit, defined in Ref. [110] as the second limit having an interacting extended $U(4) \times U(4)$ symmetry, the symmetry anomaly of TBG manifests as a perfect metal phase, where all the bands are connected to each other. A brief summary of this paper is given in Sec. VII.

II. THE BM MODEL OF TWISTED BILAYER GRAPHENE AND ITS SYMMETRIES

We first present a short review of the BM model. A more detailed account can be found in supplementary material of Ref. [56].

A. A brief review of the BM model

TBG is an engineered material of two graphene layers twisted by a small angle θ from each other. The band structure of each of the two layers exhibits two Dirac points at the K and K' momenta in the single layer BZ, respectively; the two Dirac points are related by time reversal T. Thus the band structure of TBG exhibits four Dirac points: two from the top layer and the other two from the bottom layer. When θ is small such that the interlayer coupling is smooth in real space—with a length scale much larger than the atom distances—the graphene valley (K and K') is a good quantum number of low-energy states of TBG [1]. In this case, the states around K (K') in the top layer only couple to the states around K (K') in the bottom layer. Therefore, the low-energy band structure of TBG decomposes into two independent graphene valleys, and each valley has two Dirac points originated from the two

layers, respectively. In this paper, we will focus on the valley K. The bands in the other valley K' can be obtained by acting T on the bands in the valley K.

We assume the top single graphene layer is rotated from the x direction by an angle $\frac{\theta}{2}$ (rotation axis is z). Thus the Dirac Hamiltonian around K in the top layer is $-iv_F\partial_x(\cos\frac{\theta}{2}\sigma_x-\sin\frac{\theta}{2}\sigma_y)-iv_F\partial_y(\cos\frac{\theta}{2}\sigma_y+\sin\frac{\theta}{2}\sigma_x)\approx -iv_F\partial_r\cdot\sigma+i\frac{\theta}{2}v_F\partial_r\times\sigma$, where v_F is the Fermi velocity of single-layer graphene and $\sigma=(\sigma_x,\sigma_y)$ are Pauli matrices representing the A/B sublattices of graphene. The bottom layer is rotated from the x direction by an angle $-\frac{\theta}{2}$. Correspondingly, the Dirac Hamiltonian around K in the bottom layer is $-iv_F\partial_r\cdot\sigma-i\theta v_F\partial_r\times\sigma$. The interlayer coupling is encoded in a position dependent matrix $T(\mathbf{r})$, where $\mathbf{r}=(x,y)$, such that the Hamiltonian of TBG, to linear order of θ , can be written as

$$H(\mathbf{r}) = -iv_F \left(\tau_0 \partial_{\mathbf{r}} \cdot \boldsymbol{\sigma} - \frac{\theta}{2} \tau_z \partial_{\mathbf{r}} \times \boldsymbol{\sigma} \right) + \begin{pmatrix} 0 & T(\mathbf{r}) \\ T^{\dagger}(\mathbf{r}) & 0 \end{pmatrix}.$$

Here τ_0 and τ_z are the 2×2 identity matrix and the third Pauli matrix for the layer degree of freedom, respectively. According to Ref. [1], when θ is small (\approx 1°), $T(\mathbf{r})$ forms a smooth moiré potential:

$$T(\mathbf{r}) = \sum_{i=1}^{3} e^{-i\mathbf{q}_{i}\cdot\mathbf{r}} T_{i},$$
 (2)

where \mathbf{q}_i 's are $\mathbf{q}_1 = k_D(0, -1)$, $\mathbf{q}_2 = k_D(\frac{\sqrt{3}}{2}, \frac{1}{2})$, $\mathbf{q}_3 = k_D(-\frac{\sqrt{3}}{2}, \frac{1}{2})$, with $k_D = 2|K|\sin\frac{\theta}{2}$ being the distance between K momenta in the two layers, and T_i 's are

$$T_{i} = w_{0}\sigma_{0} + w_{1} \left[\sigma_{x} \cos \frac{2\pi(i-1)}{3} + \sigma_{y} \sin \frac{2\pi(i-1)}{3} \right],$$
(3)

where w_0 and w_1 are two constant parameters. Since the w_0 term contributes to the diagonal elements, it represents the interlayer coupling between the A(B) sublattice of the top layer and the A(B) sublattice of the bottom layer. Similarly, the w_1 term only contributes to the off-diagonal elements; it is thus associated to the interlayer coupling between the A(B) sublattice of the top layer and B(A) sublattice of the bottom layer.

The moiré potential [Eq. (2)] is invariant (up to a gauge transformation) under the translations $\mathbf{a}_{M1} = \frac{2\pi}{k_D}(\frac{1}{\sqrt{3}},\frac{1}{3})$, $\mathbf{a}_{M2} = \frac{2\pi}{k_D}(-\frac{1}{\sqrt{3}},\frac{1}{3})$. The translation symmetry of the moiré potential is manifest in real space [Fig. 1(a)]. The corresponding reciprocal-lattice bases are $\mathbf{b}_{M1} = \mathbf{q}_2 - \mathbf{q}_1$, $\mathbf{b}_{M2} = \mathbf{q}_3 - \mathbf{q}_1$ [Fig. 1(b)]. The unit cell spanned by \mathbf{a}_{M1} and \mathbf{a}_{M2} is referred to as the moiré unit cell. Each moiré unit cell has one AA region, one AB region, and one BA region. In the AA region, the A(B) sublattice of the top layer sits on top of the A(B) sublattice of the bottom layer; in the AB region, the A and B sublattices of the top layer sit on top of the B sublattices and the empty hexagon centers of the bottom layer, respectively; in the BA region, the B and A sublattices of the upper layer sit on top of the A sublattices and the empty hexagon centers of the lower layer, respectively. First-principle calculations show that the two layers are corrugated

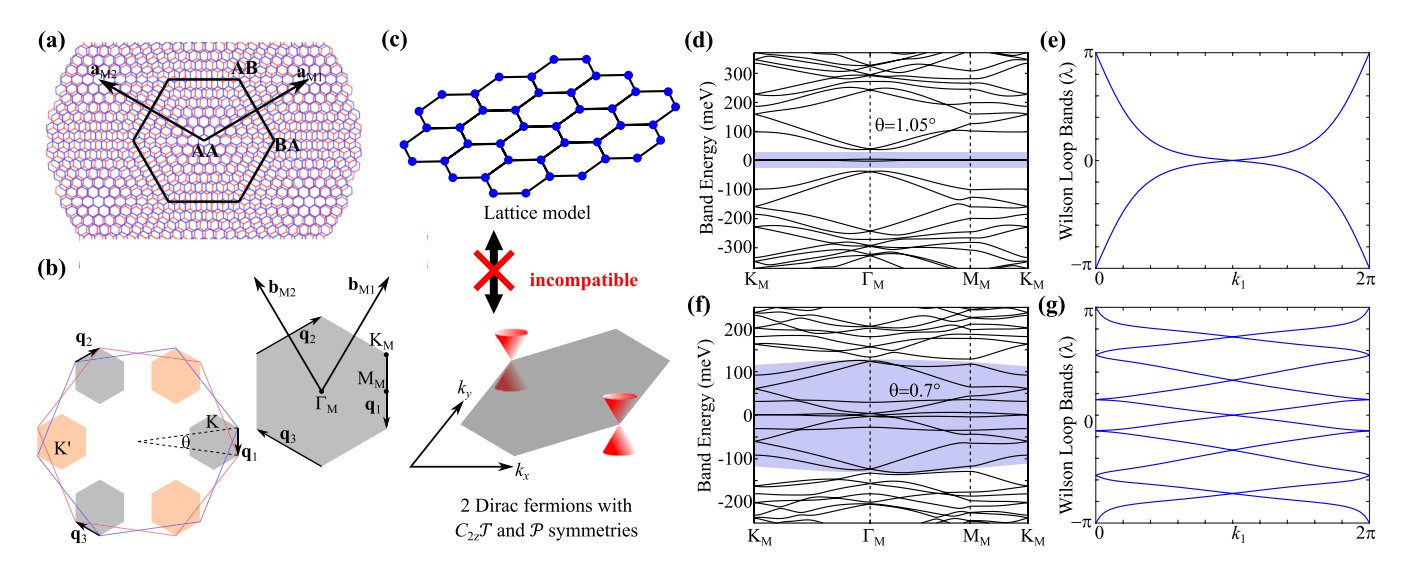


FIG. 1. The lattice, symmetry anomaly, band structures, and Wilson loop bands of TBG. (a) The moiré unit cell, where the blue sheet and the red sheet represent the top and bottom layers, respectively. In the AA, AB, and BA regions, the A sublattice of the top layer is located above the A sublattice, the B sublattice, and the hexagon center of the bottom layer, respectively. (b) The moiré Brillouin zone. Left: The gray and yellow hexagons represent the moiré Brillouin zone for the graphene valleys K and K', respectively. Right: The reciprocal lattices and the high-symmetry momenta of the moiré Brillouin zone in graphene valley K. (c) 4l + 2 ($l \in \mathbb{N}$) Dirac points cannot be realized in lattice models with $C_{2z}T$ and \mathcal{P} symmetries. (d, e) The band structure and Wilson loop bands of the middle two bands (shaded) at $\theta = 1.05^{\circ}$. The crossings in Wilson loop bands are protected by $C_{2z}T$ and/or the approximate \mathcal{P} . Each Wilson loop operator is integrated along \mathbf{b}_{M2} and the spectrum is plotted along \mathbf{b}_{M1} . (f, g) The band structure and Wilson loop bands of the middle ten bands (shaded) at $\theta = 0.7^{\circ}$. The crossings at $\lambda = 0$, π in the Wilson loop bands are protected by $C_{2z}T$ and/or by the approximate \mathcal{P} ; the double degeneracies with $\lambda \neq 0$, π at $k_1 = 0$, π are protected by the approximate \mathcal{P} . These double degeneracies guarantee Wilson loop flow for any bands with 4n + 2 Dirac nodes at zero energy. In fact, we have kept the \mathcal{P} -breaking term $i\theta v_F \tau_z \partial_{\mathbf{r}} \times \sigma$ [Eq. (1)] in the calculations used to generate this plot, which would split the double degeneracies in principle. However, the splittings are almost invisible by eye in the plot, implying that the \mathcal{P} symmetry is a good approximation. The degeneracies are exact when P is exact. The parameters of the Hamiltonian used in (d)–(g) are $v_F = 5.944$ eV Å, |K| = 1.703 Å $^{-1}$, |K| = 1.703 Å $^{-1}$, |K| = 1.703 M $^{-1}$.

in the z direction [119–122]. The distance between the two layers in the AA region is larger than the distance in the AB and BA regions. Since w_0 and w_1 are mainly dominated by the couplings in the AA and AB/BA regions [1], respectively, this implies that, in the realistic model, w_0 is smaller than w_1 [53]. In Figs. 1(d) and 1(f), we show the band structures for two different twist angles $\theta = 1.05^{\circ}$, 0.7° . The parameters are set as $v_F = 5.944$ eV Å, |K| = 1.703 Å⁻¹, $w_1 = 110$ meV, $w_0 = 0.7w_1$.

B. Symmetries of the BM model

The model Eq. (1) has several point-group symmetries: (i) $C_{2z}T = \sigma_x K$, where K is the complex conjugation, (ii) $C_{3z} = e^{i\frac{2\pi}{3}\sigma_z}$, and (iii) $C_{2x} = \tau_x\sigma_x$. One can verify that the Hamiltonian is invariant under these symmetries. Notice that the single-graphene-valley Hamiltonian does not have the C_{2z} rotation and the time-reversal T symmetries since they map one graphene valley to the other. The three crystalline symmetries and the moiré translations generate the magnetic space group P6'2'2 (no. 177.151 in the BNS setting [123]) [56].

We define a unitary particle-hole operation $P = i\tau_y$, which transforms the position as $\mathbf{r} \to -\mathbf{r}$ [56]. Here $\tau_{x,y,z}$ are Pauli matrices representing the layer degree of freedom. Under P the Hamiltonian transforms as

$$PH(\mathbf{r})P^{\dagger} = -H(-\mathbf{r}) + i\theta v_F \tau_z \partial_{\mathbf{r}} \times \mathbf{\sigma}. \tag{4}$$

The second term on the right-hand side is in linear order of θ . It approaches zero when $\theta \to 0$, while the other terms in $H(\mathbf{r})$ do not vanish in the $\theta \to 0$ limit. Thus it is safe to ignore this term in the small angle limit. To be specific, when $\theta \sim 1^{\circ}$, this term is of order $0.018v_Fk_D$ and hence is much smaller than the energy scale of the low-energy physics, which is of order v_Fk_D . Therefore, P is an emergent anticommuting symmetry when θ is small. It satisfies the algebra [56]

$$[C_{2z}T, P] = [C_{3z}, P] = 0, \{C_{2x}, P\} = 0, P^2 = -1.$$
 (5)

For later convenience, we define an antiunitary particle operation $\mathcal{P} = PC_{2z}T = i\tau_y\sigma_xK$, which is local in real space and satisfies $\mathcal{P}^2 = -1$. It acts on the Hamiltonian as

$$\mathcal{P}H(\mathbf{r})\mathcal{P}^{-1} = -H(\mathbf{r}) + i\theta v_F \tau_z \partial_{\mathbf{r}} \times \boldsymbol{\sigma}. \tag{6}$$

As discussed in detail in Appendix B, the **k** dependence in the interlayer coupling may also cause a breaking of the emergent \mathcal{P} symmetry. We can also define a chiral operation $C = \sigma_z$, which is local in real space [58]. Under C the Hamiltonian transforms as

$$CH(\mathbf{r})C^{\dagger} = -H(\mathbf{r}) + 2w_0 \tau_x \sigma_0 \sum_{i=1}^3 e^{-i\mathbf{q}_i \cdot \mathbf{r}}.$$
 (7)

In the so-called chiral limit [58], i.e., $w_0 = 0$, the second term on the right-hand side vanishes and hence C becomes an emergent anticommuting symmetry. The chiral symmetry

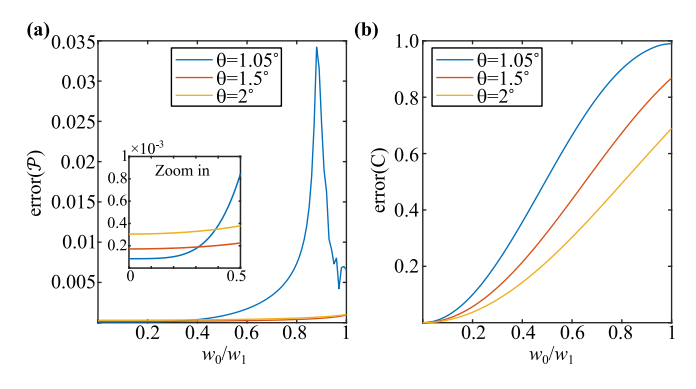


FIG. 2. Errors of the approximate symmetries \mathcal{P} (a) and C (b) on the wave functions [as defined in Eqs. (9) and (10)] in TBG as functions of w_0/w_1 . Here we change w_0 while keeping w_1 fixed (110 meV). The errors are shown for different values of the twist angle $\theta = 1.05^{\circ}$, 1.5° , 2° .

satisfies the algebra

$${C_{2z}T, C} = {C_{2x}, C} = 0, \ [C_{3z}, C] = [P, C] = 0, \ C^2 = 1.$$
(8)

We numerically checked how much \mathcal{P} and C are broken in the *wave functions* of the model Eq. (1). To be specific, we define the errors of the two symmetries in the two flatbands as

$$\operatorname{error}(\mathcal{P}) = 1 - \frac{1}{\Omega_M} \int d^2 \mathbf{k} |\langle u_{1,-\mathbf{k}} | \mathcal{P} | u_{-1,\mathbf{k}} \rangle|^2, \qquad (9)$$

$$\operatorname{error}(C) = 1 - \frac{1}{\Omega_M} \int d^2 \mathbf{k} |\langle u_{1,\mathbf{k}} | C | u_{-1,\mathbf{k}} \rangle|^2, \quad (10)$$

respectively, where $|u_{-1,\mathbf{k}}\rangle$ and $|u_{1,\mathbf{k}}\rangle$ are the periodic parts of the Bloch states of the highest occupied band and the lowest empty band at charge neutrality, respectively, and $\Omega_M = |\mathbf{b}_{M1} \times \mathbf{b}_{M2}| = \frac{3\sqrt{3}}{2}k_D^2$ is the area of the moiré Brillouin zone. When the two symmetries are exact, we have $|\langle u_{1,-\mathbf{k}}|\mathcal{P}|u_{-1,\mathbf{k}}\rangle| = |\langle u_{1,\mathbf{k}}|C|u_{-1,\mathbf{k}}\rangle| = 1$ and hence the errors are zero. Using the parameters $v_F = 5.933$ eV Å, $|K| = 1.703~\text{Å}^{-1}$, $w_1 = 110$ meV, we plot error(\mathcal{P}) and error(C) as functions of w_0/w_1 (with fixed w_1) for a few twist angles in Fig. 2. For $\theta = 1.05^\circ$, error(\mathcal{P}) is small (<0.01) for $w_0 \leqslant 0.82w_1$, thus the \mathcal{P} symmetry is a good approximation for TBG, while the C symmetry only starts being good (with error<0.01) for $w_0 \leqslant 0.07w_1$.

III. STABLE TOPOLOGY PROTECTED BY PARTICLE-HOLE SYMMETRY ${\cal P}$

A. The Wilson loop \mathbb{Z}_2 invariant protected by \mathcal{P}

We denote the Hamiltonian in momentum space as $H(\mathbf{k})$. We assume the emergent antiunitary particle-hole symmetry, i.e., $\mathcal{P}H(\mathbf{k})\mathcal{P}^{-1} = -H(-\mathbf{k})$, and $\mathcal{P}^2 = -1$. As detailed in Sec. II B, $\mathcal{P} = PC_{2z}T$ is antiunitary and squares to -1, and is the product of the unitary P of Ref. [56] and $C_{2z}T$. We denote the energy and the periodic part of the Bloch state of the nth band above (below) the zero energy as $\epsilon_n(\mathbf{k})$ [$\epsilon_{-n}(\mathbf{k})$] and $|u_n(\mathbf{k})\rangle$ [$|u_{-n}(\mathbf{k})\rangle$], respectively. As explained in Appendix A and in Ref. [56], $|u_n(\mathbf{k})\rangle$ satisfies the periodicity $|u_n(\mathbf{k} + \mathbf{G})\rangle = V^{\mathbf{G}}|u_n(\mathbf{k})\rangle$, with \mathbf{G} being a reciprocal lattice and $V^{\mathbf{G}}$ a unitary matrix referred to as the embedding matrix.

Since \mathcal{P} anticommutes with the Hamiltonian and flips the momentum, we have $\epsilon_n(\mathbf{k}) = -\epsilon_{-n}(-\mathbf{k})$. The state $\mathcal{P}|u_n(\mathbf{k})\rangle$ must have the momentum $-\mathbf{k}$ and the energy $\epsilon_{-n}(-\mathbf{k})$. In general, $\mathcal{P}|u_n(\mathbf{k})\rangle$ is spanned by Bloch states at $-\mathbf{k}$ as

$$\mathcal{P}|u_n(\mathbf{k})\rangle = \sum_{n'} |u_{n'}(-\mathbf{k})\rangle B_{n'n}^{(\mathcal{P})}(\mathbf{k}), \tag{11}$$

where the summation over n' is limited to those satisfying $\epsilon_{n'}(\mathbf{k}) = -\epsilon_n(-\mathbf{k})$, and $B_{n'n}^{(\mathcal{P})}(\mathbf{k})$ is a unitary matrix referred to as the sewing matrix of \mathcal{P} . $B^{(\mathcal{P})}(\mathbf{k})$ is periodic in momentum space, i.e., $B^{(\mathcal{P})}(\mathbf{k} + \mathbf{G}) = B^{(\mathcal{P})}(\mathbf{k})$ [124,125]. Since $\mathcal{P}^2 = -1$, it should satisfy

$$B^{(\mathcal{P})}(-\mathbf{k})B^{(\mathcal{P})*}(\mathbf{k}) = -1. \tag{12}$$

Multiplying $B^{(\mathcal{P})T}(\mathbf{k})$ on the right-hand side of the above equation, we obtain

$$B^{(\mathcal{P})}(-\mathbf{k}) = -B^{(\mathcal{P})T}(\mathbf{k}). \tag{13}$$

We now prove that the \mathcal{P} symmetry protects a \mathbb{Z}_2 invariant for 2M particle-hole symmetric separate bands, i.e., bands $\epsilon_{-M}(\mathbf{k})$, $\epsilon_{-M+1}(\mathbf{k})\cdots\epsilon_{M}(\mathbf{k})$, gapped from higher and lower bands. This proof is not limited to TBG but applies to any system having our antiunitary \mathcal{P} symmetry. We introduce the matrix $U(\mathbf{k}) = (|u_{-M}(\mathbf{k})\rangle, |u_{-M+1}(\mathbf{k})\rangle\cdots|u_{M}(\mathbf{k})\rangle)$. We parametrize \mathbf{k} as $k_1\mathbf{b}_1 + k_2\mathbf{b}_2$, where \mathbf{b}_1 and \mathbf{b}_2 are the reciprocal-lattice basis vectors. Then we define the Wilson loop operator of the 2M bands for a given k_1 as

$$W(k_1) = \lim_{N \to \infty} \prod_{i=0}^{N-1} U^{\dagger} \left(k_1, j \frac{2\pi}{N} \right) U\left(k_1, (j+1) \frac{2\pi}{N} \right). \tag{14}$$

The order of the matrices in the product is given by j: matrices with larger k_2 (= $j\frac{2\pi}{N}$) always appear on the right-hand side of matrices with smaller k_2 . Due to the periodicity of Bloch states, $W(k_1)$ is periodic. Since $W(k_1)$ is unitary, its eigenvalues are phase factors $e^{i\lambda_n(k_x)}$ ($n=1\cdots 2M$), where $\lambda_n(k_1)$ ranges from $-\pi$ to π . $\{\lambda_n(k_1)\}$ are called the Wilson loop bands. Topology is usually a result of Wilson loop flow, which in turn is a result of unavoidable crossings between Wilson loop bands.

We now prove that the Wilson loop bands are doubly degenerate at $k_1 = 0$ and π , as shown in Figs. 3(a)–3(c). In fact, we should heuristically expect this, since the Wilson loop respects \mathcal{P} as it contains all bands related by the particle-hole symmetry. Since \mathcal{P} is antiunitary and squares to -1 it hence acts as spinful time reversal, which we already know to enforce Kramers doublets in the Wilson loop spectrum [126,127]. Due to Eq. (11), we have

$$\langle u_{n}(\mathbf{k})|u_{n'}(\mathbf{k}')\rangle = \langle \mathcal{P}u_{n'}(\mathbf{k}')|\mathcal{P}u_{n}(\mathbf{k})\rangle$$

$$= \sum_{mm'} B_{m'n'}^{(\mathcal{P})*}(\mathbf{k}')\langle u_{m'}(-\mathbf{k}')|u_{m}(-\mathbf{k})\rangle B_{mn}^{(\mathcal{P})}(\mathbf{k}).$$
(15)

In the above equation we have made use of a property of antiunitary symmetries: for any two states $|\phi\rangle$ and $|\psi\rangle$ and an arbitrary antiunitary operator \mathcal{O} , we have $\langle \phi | \psi \rangle = \langle \mathcal{O} \psi | \mathcal{O} \phi \rangle$. Substituting this relation into Eq. (14) and using the periodicity relations $B^{(\mathcal{P})}(\mathbf{k} + \mathbf{G}) = B^{(\mathcal{P})}(\mathbf{k})$ and $|u_n(\mathbf{k} + \mathbf{G})\rangle =$

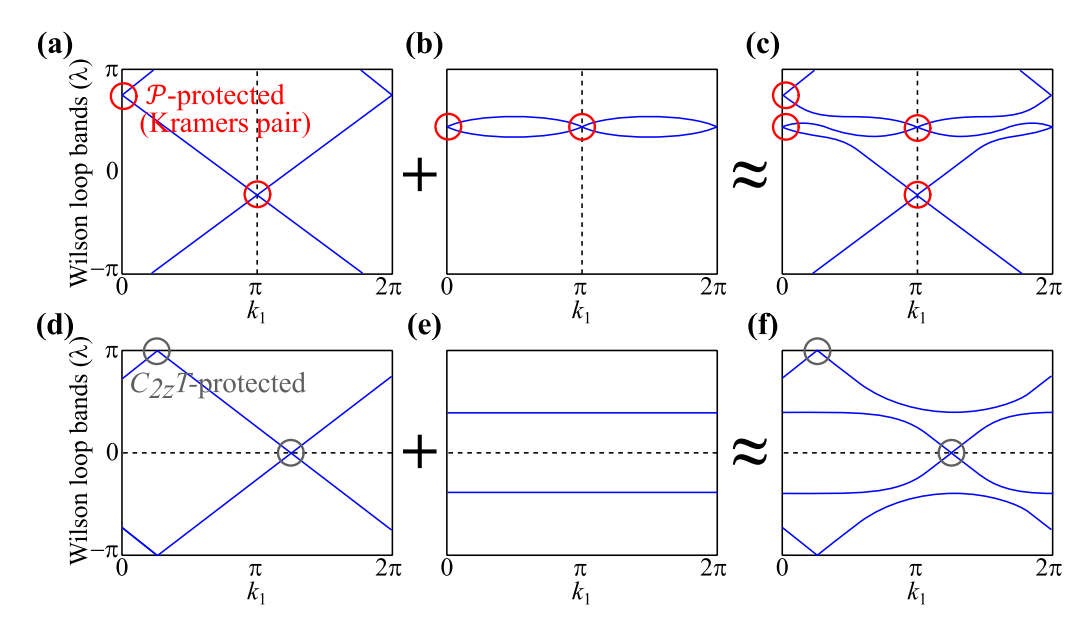


FIG. 3. Comparison of Wilson loop windings protected by \mathcal{P} and $C_{2z}T$. (a-c) The Wilson loop bands with \mathcal{P} . The crossings at $k_1=0$, π are Kramers pairs protected by \mathcal{P} . The \mathbb{Z}_2 invariant (a) equals to 1 if the Wilson loop bands form a zigzag connection between $k_1=0$ and π and (b) equals to zero otherwise. The \mathcal{P} -protected topology is stable against adding trivial bands: Coupling the nontrivial Wilson loop bands (a) to trivial Wilson loop bands (b) yields nontrivial Wilson loop bands (c). (d-f) The Wilson loop bands with $C_{2z}T$. The crossings at $\lambda=0$, π are protected by $C_{2z}T$. For a two-band system, the topology is nontrivial if the Wilson loop bands wind (d) and is trivial otherwise (e). The $C_{2z}T$ -protected topology is fragile: Coupling the nontrivial Wilson loop bands (d) to trivial Wilson loop bands (f) yields trivial Wilson loop bands (f).

 $V^{\mathbf{G}}|u_n(\mathbf{k})\rangle$, we obtain

$$W(k_1) = B^{(\mathcal{P})T}(k_1, 0)W^T(-k_1)B^{(\mathcal{P})*}(k_1, 0).$$
 (16)

Since $W(k_1)$ is periodic at $k_1, W(k_1)$ with $k_1 = 0, \pi$ are invariant under the particle-hole operation:

$$W(k_1) = B^{(\mathcal{P})T}(k_1, 0)W^T(k_1)B^{(\mathcal{P})*}(k_1, 0), \quad (k_1 = 0, \pi).$$
(17)

It is this invariance that protects degeneracies of Wilson loop bands at $k_1=0,\pi$. To see this, we parametrize the unitary matrix $W(k_1)$ as $e^{i\mathcal{H}(k_1)}$ with $\mathcal{H}(k_1)$ being a Hermitian matrix periodic in k_1 , called the Wilson Hamiltonian. The eigenvalues of $\mathcal{H}(k_1)$ form the Wilson loop bands. We can define the particle-hole operator for $\mathcal{H}(k_1)$ as $\tilde{\mathcal{P}}(k_1)=B^{(\mathcal{P})}(k_1,0)K$ such that Eq. (16) can be written as $\mathcal{H}(k_1)=\tilde{\mathcal{P}}(-k_1)\mathcal{H}(-k_1)\tilde{\mathcal{P}}^{-1}(-k_1)$. We have $\tilde{\mathcal{P}}(k_1)\tilde{\mathcal{P}}(-k_1)=-1$ due to Eq. (12). It is worth noting that unlike the Hamiltonian $H(\mathbf{k})$ which anticommutes with \mathcal{P} , $\mathcal{H}(k_1)=0$ for $k_1=0,\pi$, the Wilson loop bands—the eigenstates of the Wilson Hamiltonian—at $k_1=0,\pi$ form doublets due to the Kramers theorem.

The \mathbb{Z}_2 invariant δ is defined such that $\delta=1$ if the Wilson loop bands form a zigzag flow between $k_1=0$ and π —equivalent to a quantum spin Hall (QSH) flow of Kramers paired Wannier centers, and $\delta=0$ otherwise. Examples of $\delta=1$ and 0 with only $\mathcal P$ symmetry are shown in Figs. 3(a) and 3(b), respectively. Figure 3(a) does not contain the $C_{2z}T$ symmetry and is meant to depict the possible cases with only our antiunitary $\mathcal P$ symmetry. Because the degeneracies at $k_1=0$, π are protected by $\mathcal P$, a zigzag flow is stable against adding $\mathcal P$ -preserving bands as long as these bands are topolog-

ically trivial (they do not exhibit Wilson loop flow themselves) and do not close the gaps between the 2M bands and the higher/lower bands [Figs. 3(a)-3(c)].

In Figs. 1(e) and 1(g), we plot the Wilson loop bands of the middle two bands $(\epsilon_{-1}(\mathbf{k}), \epsilon_{1}(\mathbf{k}))$ of TBG with $\theta = 1.05^{\circ}$ and the Wilson loop bands of the middle ten bands $[\epsilon_{-5}(\mathbf{k})\cdots\epsilon_{5}(\mathbf{k})]$ of TBG with $\theta = 0.7^{\circ}$, respectively. Both have the zigzag flow and hence have $\delta = 1$. We do not plot the Wilson loop bands of the middle ten bands of TBG with $\theta = 1.05^{\circ}$ because they have touching points with higher/lower bands at generic momenta (away from high-symmetry lines).

B. Comparison of the \mathcal{P} -protected topology and $C_{2r}T$ -protected topology

In Ref. [56], some of the authors of the present paper proved that the $C_{2z}T$ symmetry protects the Wilson loop flow for two bands, as shown in Fig. 3(d), where the crossings at $\lambda = 0$, π are protected by $C_{2z}T$. The Wilson loop flow is characterized by an integer-valued invariant e_2 : the winding number of a smooth branch of the Wilson loop bands. There is a gauge ambiguity for the sign of e_2 . For example, the Wilson loop bands in Fig. 3(d) have $e_2 = 1$ if we choose the branch going up to define the winding number and $e_2 = -1$ if we choose the branch going down. e_2 is also referred to as Euler's class [54], as will be briefly introduced in Sec. V. With only $C_{2z}T$ symmetry, the flow can be broken by adding two trivial (flat) Wilson loop bands, as shown in Figs. 3(d)-3(f), since the crossings at generic positions—different from $\lambda = 0, \pi$ —in the Wilson loop spectrum are not protected by $C_{2z}T$. After the Wilson loop bands are gapped, one can still define a $C_{2z}T$ protected \mathbb{Z}_2 invariant through the nested Wilson loop [54,56].

Nevertheless, this $C_{2z}T$ -protected \mathbb{Z}_2 invariant does not correspond to Wannier obstruction [54,55]. Therefore, the topology protected only by $C_{2z}T$ is fragile. Reference [56] showed that, by adding the unitary particle-hole symmetry P, one cannot render the Stiefel-Whitney class [54] trivial by adding more bands; however, the nontrivial Stiefel-Whitney index does not imply non-Wannierizable bands, and hence Ref. [56] called the index "stable," between quotation marks; this paper removes the quotation marks by proving non-Wannierizability.

In contrast, with the \mathcal{P} symmetry, we cannot break the zigzag flow by adding trivial (nonwinding) Wilson loop bands, just like in the quantum spin Hall problem. First, due to the Kramers degeneracy guaranteed by \mathcal{P} , a trivial state must have at least two Wilson loop bands—corresponding to the fact that, with particle-hole symmetry, we must add to the nontrivial bands, generically, two bands—of some energy $\pm E$. The two Wilson loop bands are separated at generic k_1 but degenerate at $k_1=0,\pi$, as shown in Fig. 3(b). If we couple such a two-band trivial state to the topological state, the total Wilson loop bands are still gapless [Fig. 3(c)] since the degeneracies at $k_1=0,\pi$ are protected. Therefore, the topology protected by \mathcal{P} is stable.

If a two-band system has both $C_{2z}T$ and \mathcal{P} symmetries, the \mathbb{Z}_2 invariant protected by \mathcal{P} is given by the parity of e_2 , i.e., $\delta = e_2 \mod 2$. For example, the Wilson loop bands in Fig. 1(e) have $e_2 = 1$ and $\delta = 1$. There is stable topology from \mathcal{P} , in systems with an even number of bands. TBG has an even number of bands (as it has to, since $\mathcal{P} = C_{2z}TP$ implies an even number of bands: nonzero energy $E \neq 0$ states come in pairs $\pm E$, while zero energy states have Kramers degeneracy since $\mathcal{P}^2 = -1$); furthermore, these bands exhibit 4l + 2 ($l \in \mathbb{N}$) Dirac nodes at zero energy (proved in Sec. IV), which will show that TBG is in the topologically nontrivial class of this symmetry.

C. An alternative expression of the \mathbb{Z}_2 invariant

We have mentioned that the zigzag flow of the Wilson loop bands protected by \mathcal{P} is the same as the zigzag flow of Wilson loop bands protected by the time-reversal symmetry in a two-dimensional (2D) quantum spin Hall topological insulator [126]. Now we show that they are indeed equivalent. Suppose $H(\mathbf{k})$ have the $\mathcal{P}(\mathcal{P}^2 = -1)$ symmetry, i.e., $H(\mathbf{k}) =$ $-\mathcal{P}H(-\mathbf{k})\mathcal{P}^{-1}$, then we define the squared Hamiltonian as $H^2(\mathbf{k}) = H(\mathbf{k}) \cdot H(\mathbf{k})$ such that it commutes with \mathcal{P} , i.e., $H^2(\mathbf{k}) = \mathcal{P}H^2(-\mathbf{k})\mathcal{P}^{-1}$. We can regard \mathcal{P} as a "time-reversal symmetry" of $H^2(\mathbf{k})$. An eigenstate of $H(\mathbf{k})$ with the energy $\epsilon_n(\mathbf{k})$ is still an eigenstate of $H^2(\mathbf{k})$ but has the squared energy $\epsilon_n^2(\mathbf{k})$. States of the 2M particle-hole-symmetric bands used to define the Wilson loop [Eq. (14)], i.e., $|u_{-M}(\mathbf{k})\rangle \cdots |u_{M}(\mathbf{k})\rangle$, form the lowest 2M bands of the squared Hamiltonian $H^2(\mathbf{k})$. Thus the Wilson loop operator of the 2M particle-hole symmetric bands of $H(\mathbf{k})$ is the same as the Wilson loop operator of the 2M lowest bands of $H^2(\mathbf{k})$. The zigzag flow of the Wilson loop can be equivalently thought of as protected by the time-reversal symmetry of $H^2(\mathbf{k})$.

The time-reversal-protected \mathbb{Z}_2 invariant can be alternatively expressed as a topological obstruction [128,129]. Consider 2M bands $\{|u_n^{\rm I}(\mathbf{k})\rangle, |u_n^{\rm II}(\mathbf{k})\rangle | n=1\cdots M\}$ in a time-reversal (\mathcal{T}) symmetric system that satisfy the gauge

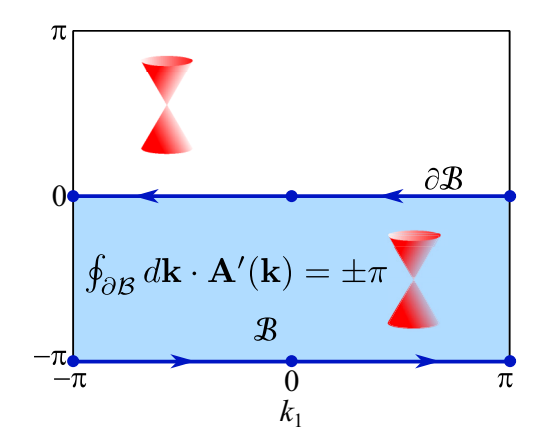


FIG. 4. The path used to define the \mathbb{Z}_2 invariant protected by \mathcal{P} . $\mathcal{B} = [-\pi, \pi] \otimes [-\pi, 0]$ is half of the Brillouin zone. Its boundary $\partial \mathcal{B}$ is invariant under the particle-hole symmetry $\mathcal{P}(\mathbf{k} \to -\mathbf{k})$. With the $C_{2z}T$ symmetry, one Dirac point in \mathcal{B} contributes to a π Berry phase along $\partial \mathcal{B}$.

condition $|u_n^{\mathrm{II}}(-\mathbf{k})\rangle = \mathcal{T}|u_n^{\mathrm{I}}(\mathbf{k})\rangle, \quad |u_n^{\mathrm{I}}(-\mathbf{k})\rangle = -\mathcal{T}|u_n^{\mathrm{II}}(\mathbf{k})\rangle,$ then the corresponding \mathbb{Z}_2 invariant is given by

$$\delta = \frac{1}{2\pi} \left(\oint_{\partial \mathcal{B}} d\mathbf{k} \cdot \mathbf{A}(\mathbf{k}) - \int_{\mathcal{B}} d^2 \mathbf{k} \, \Omega(\mathbf{k}) \right) \mod 2, \quad (18)$$

where \mathcal{B} is half of the BZ the boundary $\partial \mathcal{B}$ of which is \mathcal{P} invariant,

$$\mathbf{A}(\mathbf{k}) = i \sum_{n=1}^{M} \sum_{a=LH} \left\langle u_n^a(\mathbf{k}) \middle| \partial_{\mathbf{k}} u_n^a(\mathbf{k}) \right\rangle \tag{19}$$

is Berry's connection of the considered bands, and $\Omega(\mathbf{k}) = \partial_{\mathbf{k}} \times \mathbf{A}(\mathbf{k})$ is Berry's curvature. An example of \mathcal{B} is shown in Fig. 4. We regard $|u_{-M}(\mathbf{k})\rangle \cdots |u_{M}(\mathbf{k})\rangle$ as the lowest 2M bands of $H^{2}(\mathbf{k})$ and \mathcal{P} as the time-reversal symmetry of $H^{2}(\mathbf{k})$. If we impose the gauge $|u_{-n}(-\mathbf{k})\rangle = \mathcal{P}|u_{n}(\mathbf{k})\rangle$ ($n = 1 \cdots M$), i.e., choose the sewing matrix defined in Eq. (11) as $B_{n',n}^{(\mathcal{P})}(\mathbf{k}) = \delta_{n',-n} \mathrm{sgn}(n)$, then we can regard $|u_{n}(\mathbf{k})\rangle$ and $|u_{-n}(\mathbf{k})\rangle$ as $|u_{n}^{1}(\mathbf{k})\rangle$ and $|u_{n}^{1}(\mathbf{k})\rangle$, respectively. Thus the \mathbb{Z}_{2} invariant of the 2M bands of $H(\mathbf{k})$ protected by \mathcal{P} is given by Eq. (18). This expression will be used for one of the ways to prove the symmetry anomaly of 4l + 2 Dirac points in systems with $C_{2z}T$ and \mathcal{P} symmetries (see Sec. IV).

IV. A NO-GO THEOREM OF TWO DIRAC FERMIONS ON LATTICES WITH $C_{2z}T$ and $\mathcal P$ symmetries

In this section, we will prove that if there are 4l+2 ($l \in \mathbb{N}$) Dirac fermions at zero energy (chemical potential) in a system with $C_{2z}T$ and \mathcal{P} symmetries, then the \mathbb{Z}_2 invariant of the 2M bands (arbitrary M) above and below the chemical potential, i.e., $\epsilon_{-M}(\mathbf{k})\cdots\epsilon_{M}(\mathbf{k})$, is guaranteed to be 1, provided that the 2M bands are gapped from other bands. As a consequence, for arbitrary M, the 2M particle-hole symmetric bands are not Wannierizable. That means the 4l+2 Dirac fermions do not have a lattice support.

Before going into a mathematical proof, we first give an intuitive proof that the Wilson loop of a $C_{2z}T$ and \mathcal{P} system

with 4l + 2 Dirac fermions at zero energy needs to wind. We first assume that we have two bands separate from other bands close to charge neutrality. In Refs. [44,54] it was shown that the number of Dirac points in half BZ mod 2 equals the winding of the Wilson loop. For 4l + 2 Dirac nodes in between these two bands, the winding would be odd, as in Fig. 1(e). Adding nonzero trivial or nontrivial energy bands to this system would happen in pairs; introducing a set (trivial, due to $C_{2z}T$, which renders Chern numbers to be zero and hence makes any single band topologically trivial) of bands at nonzero energy would have its \mathcal{P} conjugate and appear in numbers 2n. Introducing nontrivial bands at nonzero energy would mean introducing $2 \times 2n$ bands into the system, as any possible nontrivial set of bands at a given energy comes as a multiple of 2. These bands can introduce only a multiple of 4 number of Dirac fermions into the system: each set of two separate bands has to have a multiple of 2 Dirac fermions. From our QSH experience, whatever number of bands we introduce on top of our nontrivial bands with 4l + 2 Dirac fermions cannot change the Wilson loop winding, as we are adding either trivial bands or pairs of nontrivial bands to a QSH system. Hence the winding (of the 4n + 2 Dirac fermion band) is stable to the addition of any bands respecting $C_{2z}T$ and \mathcal{P} . The *only* way the winding can be interrupted is by the addition of *one* set of two bands with Wilson loop winding to the already existent Wilson loop winding two bands. However, since with $C_{2z}T$ the number of Dirac nodes mod 4 is equal to twice the winding, this additional one set of two bands would bring about another 4l' + 2 Dirac points so the full system would have a number of Dirac fermions divisible by 4. Hence a system with 4l + 2 Dirac fermions and $C_{2z}T$ and \mathcal{P} has to exhibit Wilson loop winding.

Now, by making use of Eq. (18), we give another proof that 2M bands (gapped from other bands) with $C_{2z}T$ and \mathcal{P} symmetries that have 4l+2 Dirac points between $\epsilon_{-1}(\mathbf{k})$ and $\epsilon_1(\mathbf{k})$ must have a nontrivial topology. Due to the $C_{2z}T$ symmetry, the Bloch states satisfy

$$C_{2z}T|u_n(\mathbf{k})\rangle = \sum_{n'} |u_{n'}(\mathbf{k})\rangle B_{n'n}^{(C_{2z}T)}(\mathbf{k}), \qquad (20)$$

where $B_{n'n}^{(C_2zT)}(\mathbf{k})$ is unitary and called the $C_{2z}T$ sewing matrix. The summation over n' is limited to values satisfying $\epsilon_{n'}(\mathbf{k}) = \epsilon_n(\mathbf{k})$. Substituting this constraint into the definition of Berry's curvature $\Omega(\mathbf{k})$, we find that $\Omega(\mathbf{k}) = 0$ [44,54,80]. Thus we only need to evaluate the first term on the right-hand side of Eq. (18). We define $\mathbf{A}'(\mathbf{k}) = i \sum_{n=1}^{M} \langle u_n(\mathbf{k}) | \partial_{\mathbf{k}} u_n(\mathbf{k}) \rangle$ for the positive bands and $\mathbf{A}''(\mathbf{k}) = i \sum_{n=1}^{M} \langle u_n(\mathbf{k}) | \partial_{\mathbf{k}} u_n(\mathbf{k}) \rangle$ for the negative bands. The total Berry connection is $\mathbf{A} = \mathbf{A}' + \mathbf{A}''$. By imposing the gauge condition $|u_{-n}(-\mathbf{k})\rangle = \mathcal{P}|u_n(\mathbf{k})\rangle$ $(n = 1 \cdots M)$ required by Eq. (18), we find

$$\mathbf{A}''(\mathbf{k}) = i \sum_{n=1}^{M} \langle u_{-n}(\mathbf{k}) | \partial_{\mathbf{k}} u_{-n}(\mathbf{k}) \rangle$$
$$= i \sum_{n=1}^{M} \langle \partial_{\mathbf{k}} \mathcal{P} u_{-n}(\mathbf{k}) | \mathcal{P} u_{-n}(\mathbf{k}) \rangle$$

$$= i \sum_{n=1}^{M} \langle \partial_{\mathbf{k}} u_n(-\mathbf{k}) | u_n(-\mathbf{k}) \rangle$$

$$= -i \sum_{n=1}^{M} \langle u_n(-\mathbf{k}) | \partial_{\mathbf{k}} u_n(-\mathbf{k}) \rangle = \mathbf{A}'(-\mathbf{k}), \qquad (21)$$

where we have applied the property of antiunitary symmetry introduced below Eq. (15). Since the boundary $\partial \mathcal{B}$ (Fig. 4) is invariant under $\mathbf{k} \to -\mathbf{k}$, the integrals of $\mathbf{A}'(\mathbf{k})$ and $\mathbf{A}''(\mathbf{k})$ are equal, i.e.,

$$\oint_{\partial \mathcal{B}} d\mathbf{k} \cdot \mathbf{A}''(\mathbf{k}) = \oint_{\partial \mathcal{B}} d\mathbf{k} \cdot \mathbf{A}'(\mathbf{k}). \tag{22}$$

The $C_{2z}T$ symmetry stabilizes 2D Dirac points [130], and each Dirac point between the positive bands and the negative bands contributes to a π or $-\pi$ Berry phase of $\mathbf{A}'(\mathbf{k})$ (Fig. 4). Due to the \mathcal{P} symmetry $\epsilon_{-n}(-\mathbf{k}) = -\epsilon_n(\mathbf{k})$, the Dirac points must be equally distributed in \mathcal{B} and its complementary set BZ— \mathcal{B} . Hence if there are 4l+2 Dirac points in the BZ, there will be 2l+1 Dirac points in \mathcal{B} and we have $\oint_{\partial \mathcal{B}} d\mathbf{k} \cdot \mathbf{A}'(\mathbf{k}) = (2l+1)\pi$ mod 2π . According to Eq. (22), we have

$$\oint_{\partial \mathcal{B}} d\mathbf{k} \cdot (\mathbf{A}'(\mathbf{k}) + \mathbf{A}''(\mathbf{k})) = (4l + 2)\pi \mod 4\pi. \quad (23)$$

Substituting this equation into Eq. (18) and using the fact that $\Omega(\mathbf{k}) = 0$, we obtain $\delta = 1$. Thus the presence of 4l + 2Dirac points in a system with $C_{2z}T$ and \bar{P} symmetries implies a nontrivial topology. In contrast to lattice models the whole bands of which are trivial, this nontrivial topology is guaranteed by the Dirac points between $\epsilon_1(\mathbf{k})$ and $\epsilon_{-1}(\mathbf{k})$ and hence cannot be trivialized by adding higher- and lowerenergy bands (preserving \mathcal{P}). Therefore, no matter how many high-energy bands are included, as long as they respect $C_{2z}T$ and \mathcal{P} , the considered bands must have nontrivial topology. As will be shown in the next paragraph, in a lattice model with a finite number of orbitals per unit cell, the Wilson loop bands of the whole bands must be trivial. Therefore, 4l + 2Dirac points cannot be realized in lattice models because the corresponding band structure, no matter how many highand low-energy bands are considered, must be topologically nontrivial.

Here we show that the whole bands of a lattice model must be trivial. Let the lattice model have N orbitals, then the $U(\mathbf{k})$ matrix entering the Wilson loop operator [Eq. (14)] of the whole bands is $U(\mathbf{k}) = (|u_1(\mathbf{k})\rangle \cdots |u_N(\mathbf{k})\rangle)$. By the completeness of all the Bloch states we have $U(\mathbf{k})U^{\dagger}(\mathbf{k}) = 1$. Thus the Wilson loop operator in Eq. (14) is $W(k_1) = U^{\dagger}(k_1, 0)U(k_1, 2\pi) = U^{\dagger}(k_1, 0)V^{(0,2\pi)}U(k_1, 0)$, where $V^{(0,2\pi)}$ is the embedding matrix defined in Appendix A (with $\mathbf{G} = 2\pi \mathbf{b}_2$). Since $U(k_1, 0)$ is an $N \times N$ unitary matrix, the eigenvalues of $W(k_1)$ are the same as eigenvalues of $V^{(0,2\pi)}$ and hence do not change with k_1 and do not wind.

It is worth noting that, in TBG, the symmetry anomaly does not depend on the parameters of the Hamiltonian Eq. (1). In the weak-coupling limit ($w_0 \ll v_F k_D$, $w_1 \ll v_F k_D$), we have two Dirac points at K_M and K_M' in the moiré BZ. If the 2M bands $\epsilon_{-M}(\mathbf{k})\cdots\epsilon_{M}(\mathbf{k})$ are gapped from the other bands, the 2M bands must be topological due to correspondence between the number of Dirac points and the \mathbb{Z}_2 invariant δ .

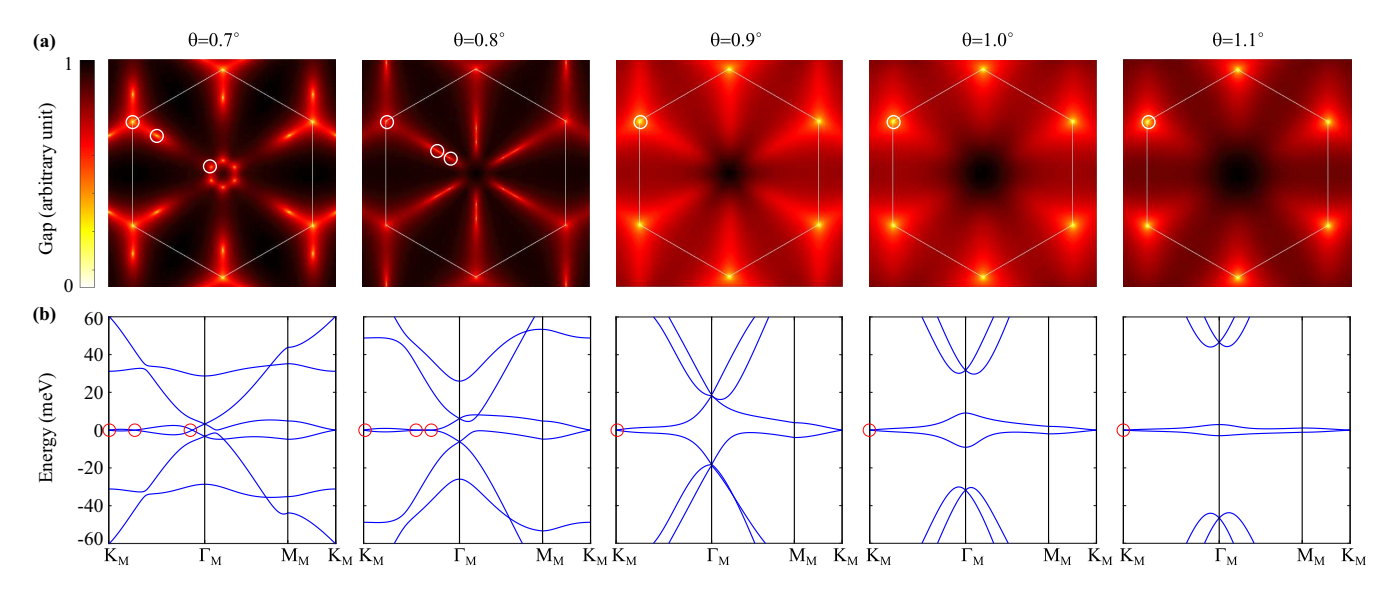


FIG. 5. The distribution of Dirac points in the moiré Brillouin zone at different twisting angles. (a) The gap between the middle two bands in the moiré Brillouin zone at $\theta = 0.7^{\circ}$, 0.8° , 0.9° , 1.0° , 1.1° , where the Dirac points along $K_M\Gamma_M$ are marked by the white circles. (b) The corresponding band structures at these twisting angles, where the Dirac points are marked by the red circles. For $\theta \ge 0.9^{\circ}$, there are two Dirac points located at K_M and K_M' , respectively, in the moiré Brillouin zone. For $\theta \le 0.8^{\circ}$, there are 14 Dirac points in the moiré Brillouin zone.

Tuning the parameters of TBG may couple the 2M bands to higher bands $\epsilon_{M+1}(\mathbf{k})\cdots\epsilon_{M'}(\mathbf{k})$ (M'>M) and lower bands $\epsilon_{-M'}(\mathbf{k})\cdots\epsilon_{-M-1}(\mathbf{k})$, which are assumed to be gapped from $\epsilon_{M'+1}(\mathbf{k})$ and $\epsilon_{-M'-1}(\mathbf{k})$ as we tune the parameters. In the weak-coupling limit, the additional 2M'-2M bands must have $\delta=0$ since they do not have Dirac points between $\epsilon_{-M-1}(\mathbf{k})$ and $\epsilon_{M+1}(\mathbf{k})$. Therefore, after we couple the 2M bands to the 2M'-2M bands, the 2M' bands as a whole will have $\delta=1+0=1$. As we tune the parameters, additional Dirac points between $\epsilon_1(\mathbf{k})$ and $\epsilon_{-1}(\mathbf{k})$ may be created due to gap closing and reopening between $\epsilon_1(\mathbf{k})$ and $\epsilon_{-1}(\mathbf{k})$. However, the total number of Dirac points between $\epsilon_1(\mathbf{k})$ and $\epsilon_{-1}(\mathbf{k})$ must equal to 2 4, i.e., 4l+2 ($l\in\mathbb{N}$), because the topological invariant of the 2M' bands is guaranteed to be $\delta=1$

In Fig. 5, we show the evolution of Dirac points with the twisting angle changing from 0.7° to 1.1° . For $\theta \in [0.9^{\circ}, 1.1^{\circ}]$, there are only two Dirac points in the moiré Brillouin zone and they locate at K_M and K'_M , respectively. When θ decreases to 0.8° , two additional Dirac points are generated along the high-symmetry line $K_M\Gamma_M$. Due to the C_{3z} and $\mathcal P$ symmetries, there are 12 Dirac points generated along the equivalent paths of $K_M\Gamma_M$. Thus for $\theta \in [0.7^{\circ}, 0.8^{\circ}]$, there are in total 14 Dirac points in the Brillouin zone. Therefore, we always have 4l + 2 ($l \in \mathbb{N}$) Dirac points: for $\theta \in [0.9^{\circ}, 1.1^{\circ}]$ l = 0 and for $\theta \in [0.7^{\circ}, 0.8^{\circ}]$ l = 3.

V. THE CHERN BAND BASIS

In this section we show that, if the two bands $\epsilon_{-1}(\mathbf{k})$ and $\epsilon_{1}(\mathbf{k})$ are gapped from other bands, we can recombine them as two Chern bands with Chern numbers e_{2} and $-e_{2}$, with e_{2} being Euler's class [54,131–133] (or, equivalently, the Wilson loop winding number protected by $C_{2z}T$ [44]). (In TBG, the Chern numbers given by $\pm e_{2}$ are also equal to the $e_{Y} = \pm 1$ index defined in Ref. [110], which, in a certain gauge, repre-

sents the eigenvalue of the Pauli y matrix in the 2D space of $n = \pm 1$ band indices).

In order to introduce the Chern band basis, we first introduce the definition of Euler's class e_2 . (We refer the readers to Refs. [44,54,131] for more details). Suppose the two bands $\epsilon_1(\mathbf{k})$ and $\epsilon_{-1}(\mathbf{k})$ are gapped from other bands. Then, at \mathbf{k} away from Dirac points between the two bands, the $C_{2z}T$ operator leaves each band unchanged up to a phase factor. In other words, the $C_{2z}T$ sewing matrix [Eq. (20)] is diagonal at these \mathbf{k} . Hence in general, the $C_{2z}T$ symmetry acts on the Bloch states as $C_{2z}T|u_n(\mathbf{k})\rangle = |u_n(\mathbf{k})\rangle e^{i\theta_n(\mathbf{k})}$ $(n=\pm 1)$, with $\theta_n(\mathbf{k})$ being the phase factors. According to Ref. [54], it follows that the non-Abelian Berry connection of the two bands at \mathbf{k} away from Dirac points takes the form

$$\mathcal{A}_{nn'}(\mathbf{k}) = i \langle u_n(\mathbf{k}) | \partial_{\mathbf{k}} u_{n'}(\mathbf{k}) \rangle$$

$$= \begin{pmatrix} -\frac{1}{2} \partial_{\mathbf{k}} \theta_1(\mathbf{k}) & -i \mathbf{a}(\mathbf{k}) e^{i \frac{\theta_1(\mathbf{k}) - \theta_{-1}(\mathbf{k})}{2}} \\ i \mathbf{a}(\mathbf{k}) e^{i \frac{\theta_{-1}(\mathbf{k}) - \theta_1(\mathbf{k})}{2}} & -\frac{1}{2} \partial_{\mathbf{k}} \theta_{-1}(\mathbf{k}) \end{pmatrix}_{nn'}. (24)$$

 $\mathbf{a}(\mathbf{k})$ is a gauge invariant quantity up to a global ambiguity of \pm sign. Euler's class is given by

$$e_2 = \frac{1}{2\pi} \sum_{i} \oint_{\partial D_i} d\mathbf{k} \cdot \mathbf{a}(\mathbf{k}) = \frac{1}{2\pi} \int_{BZ'} d^2 \mathbf{k} f(\mathbf{k}) \in \mathbb{Z}.$$
(25)

Here *i* indexes the Dirac points in the BZ, D_i is a sufficiently small region covering the *i*th Dirac point, BZ' = BZ $-\sum_i D_i$, and $f(\mathbf{k}) = \partial_{\mathbf{k}} \times \mathbf{a}(\mathbf{k})$.

In the above we have assumed that the $|u_n(\mathbf{k})\rangle$ is smooth over the Brillouin zone *except* at the Dirac points. Equation (24) is valid only in this gauge. In this gauge $\theta_n(\mathbf{k})$ is necessarily \mathbf{k} dependent if there exist Dirac points between the *n*th band and other bands. Since each Dirac point contributes to a π Berry phase, there must be $2\oint_{\partial D_i}d\mathbf{k}\cdot\mathcal{A}_{nn}(\mathbf{k})=\oint_{\partial D_i}d\mathbf{k}\cdot\partial_{\mathbf{k}}\theta_n(\mathbf{k})=2\pi\mod 4\pi$. Thus $\theta_n(\mathbf{k})$ must wind odd times around a Dirac point.

We introduce the two Chern band bases as

$$|v_{\pm}(\mathbf{k})\rangle = \frac{1}{\sqrt{2}} \left(e^{i\frac{\theta_1(\mathbf{k})}{2}} |u_1(\mathbf{k})\rangle \pm i e^{i\frac{\theta_{-1}(\mathbf{k})}{2}} |u_{-1}(\mathbf{k})\rangle \right). \tag{26}$$

There are two ambiguities in the above equation.

(i) There is an ambiguity of the two branches of $\frac{\theta_n}{2}$, i.e., $\frac{\theta_n}{2}$ and $\frac{\theta_n}{2} + \pi$.

(ii) At the Dirac points, where the two bands are degenerate, there is an ambiguity of choosing $u_1(\mathbf{k})$ and $u_{-1}(\mathbf{k})$.

Replacing $\theta_1(\mathbf{k})/2$ by $\theta_1(\mathbf{k})/2 + \pi$ or replacing $\theta_{-1}(\mathbf{k})/2$ by $\theta_{-1}(\mathbf{k})/2 + \pi$ will interchange $|v_+(\mathbf{k})\rangle$ with $|v_-(\mathbf{k})\rangle$. Similarly, interchanging $|u_1(\mathbf{k})\rangle$ and $|u_{-1}(\mathbf{k})\rangle$ at the Dirac points will also interchange $|v_+(\mathbf{k})\rangle$ with $|v_-(\mathbf{k})\rangle$ at the Dirac points. To solve these ambiguities, as detailed in Appendix C, we require Berry's curvatures of $|v_+(\mathbf{k})\rangle$ and $|v_-(\mathbf{k})\rangle$ to be continuous, or, equivalently,

$$\lim_{\mathbf{q} \to 0} |\langle v_{m'}(\mathbf{k} + \mathbf{q}) | v_m(\mathbf{k}) \rangle| = \delta_{m'm}, \tag{27}$$

where $m, m' = \pm$. Using Eqs. (24) and (26), we can calculate the non-Abelian Berry connection on the basis $|v_{\pm}(\mathbf{k})\rangle$ at \mathbf{k} away from the Dirac points. We obtain

$$\mathcal{A}'_{mm'}(\mathbf{k}) = i \langle v_m(\mathbf{k}) | \partial_{\mathbf{k}} v_{m'}(\mathbf{k}) \rangle = \begin{pmatrix} \mathbf{a}(\mathbf{k}) & 0 \\ 0 & -\mathbf{a}(\mathbf{k}) \end{pmatrix}_{mm'}, (28)$$

and hence

$$\mathcal{F}'_{mm'} = -\begin{bmatrix} \partial_{k_x} - \mathcal{A}'_x, \, \partial_{k_y} - \mathcal{A}'_y \end{bmatrix}_{mm'} = \begin{pmatrix} f(\mathbf{k}) & 0 \\ 0 & -f(\mathbf{k}) \end{pmatrix}_{\substack{mm' \\ (29)}},$$

for **k** not at the Dirac points. Therefore, if Berry's curvature does not diverge at Dirac points, which is true as shown in the next paragraph, the Chern numbers of the states $|v_{\pm}(\mathbf{k})\rangle$ are

$$C_{\pm} = \pm \frac{1}{2\pi} \int d^2 \mathbf{k} \, f(\mathbf{k}) = \pm e_2.$$
 (30)

To conclude this section, we show that in the chiral limit $w_0 = 0$ the Chern band basis can be chosen as the eigenstates of the chiral symmetry C [Eq. (7)]. We define the sewing matrix of C as

$$C|u_n(\mathbf{k})\rangle = \sum_{n'} |u_{n'}(\mathbf{k})\rangle B_{n'n}^{(C)}(\mathbf{k}), \tag{31}$$

where the summation over n' satisfies $\epsilon_{n'}(\mathbf{k}) = -\epsilon_n(\mathbf{k})$. For the TBG Hamiltonian Eq. (1), the $C_{2z}T$ and C operators are $\sigma_x K$ and σ_z , respectively. Thus we have the algebra $C^2 = 1$ and $\{C, C_{2z}T\} = 0$ and hence

$$[B^{(C)}(\mathbf{k})]^2 = 1,$$
 (32)

$$B^{(C_{2z}T)}(\mathbf{k})B^{(C)*}(\mathbf{k}) + B^{(C)}(\mathbf{k})B^{(C_{2z}T)}(\mathbf{k}) = 0.$$
 (33)

As discussed at the beginning of this section, at **k** not at the Dirac points, we have $B_{n'n}^{(C_{2z}T)}(\mathbf{k}) = \delta_{n'n}e^{i\theta_n(\mathbf{k})}$. Then the solution of $B^{(C)}(\mathbf{k})$ is

$$B^{(C)}(\mathbf{k}) = \pm \begin{pmatrix} 0 & -ie^{i\frac{\theta_1(\mathbf{k}) - \theta_{-1}(\mathbf{k})}{2}} \\ ie^{i\frac{\theta_{-1}(\mathbf{k}) - \theta_1(\mathbf{k})}{2}} & 0 \end{pmatrix}.$$
(34)

The \pm sign cannot be determined by solving Eqs. (32) and (33). In practice, one should evaluate Eq. (31) to determine the \pm sign for given $|u_{\pm 1}(\mathbf{k})\rangle$. We find that the

Chern band basis Eq. (26) diagonalizes $B^{(C)}(\mathbf{k})$. Below Eq. (26) we have discussed the ambiguity of choosing $|v_{\pm}(\mathbf{k})\rangle$ and we have imposed Eq. (27) to fix this ambiguity. This ambiguity of Eq. (26) can be alternatively solved by choosing $|v_{\pm}(\mathbf{k})\rangle$ as the eigenstates of C with the eigenvalues ± 1 , respectively. This choice automatically satisfies Eq. (27) since the states with different chiral eigenvalues are orthogonal, i.e., $\langle v_{-}(\mathbf{k})|v_{+}(\mathbf{k}')\rangle = \langle v_{-}(\mathbf{k})|C^{\dagger}C|v_{+}(\mathbf{k}')\rangle = -\langle v_{-}(\mathbf{k})|v_{+}(\mathbf{k}')\rangle = 0$ for arbitrary \mathbf{k} and \mathbf{k}' .

The Chern band basis in Eq. (26) can also be equivalently defined through the Wilson loop method [29,86]. Besides, in the chiral limit, the Chern band basis we defined is equivalent to that defined in [19].

VI. PERFECT METAL PHASE OF TWISTED BILAYER GRAPHENE IN THE SECOND CHIRAL LIMIT

In our paper Ref. [110], we consider the opposite limit of the usual chiral limit: Instead of letting $w_0 = 0$, we take w_1 to be zero. When $w_1 = 0$, the model Eq. (1) has another chiral symmetry $C' = \tau_z \sigma_z$ acting on the Hamiltonian as $C'H(\mathbf{r})C'^{\dagger} = -H(\mathbf{r})$. Thus we call this limit the second chiral limit. As discussed in Sec. II A, w_0 and w_1 are the interlayer couplings contributed mainly by the AA and AB/BA regions, respectively; thus the second chiral limit can be (approximately) realized if the layer distance in the AA region is smaller than the layer distance in the AB and BA regions (shorter distance means stronger coupling). Such a configuration would be different from the corrugation predicted by the first-principle calculations [119–122], where the distance in the AA region is larger. Nevertheless, the second chiral limit could potentially be engineered by putting the TBG on a certain substrate, and it represents an interesting interacting limit [110]. We are mainly interested in the novel electronic band structure of TBG in the second chiral limit and hence we leave the material realization of the second chiral limit for future study.

We find that, in the second chiral limit, the nth positive (negative) band is always connected to the (n+1)th positive (negative) band. As the first positive band and the first negative band are connected through the Dirac points, the whole bands are all connected, as shown in Fig. 6(a). The phase with all bands connected is referred to as the perfect metal [134] in trilayer systems, where the number of Dirac nodes is odd. In the current case, we also find this "perfect metal" in an even number of Dirac node systems with the special chiral symmetry of the second chiral limit.

The perfect metal phase is protected by $C_{2z}T$, P, and C'. The new chiral symmetry C' has a strange group algebra as it anticommutes with T and with P [111]. We define the product of P and C' as an effective inversion symmetry $I = PC' = \tau_x \sigma_z$. It commutes with the Hamiltonian, i.e., $H(-\mathbf{r}) = IH(\mathbf{r})I^{\dagger}$ and $H(-\mathbf{k}) = IH(\mathbf{k})I^{\dagger}$ accordingly. The effective inversion operator satisfies the algebra

$${C_{2z}T, I} = 0,$$
 ${P, I} = 0,$ ${I^2 = 1.}$ (35)

We first show that $C_{2z}T$ and I protect double degeneracies at I-invariant momenta. (In TBG, the I-invariant momenta are Γ_M and the three equivalent M_M). Since the Hamiltonian at an I-invariant momentum commutes with I, the Bloch states

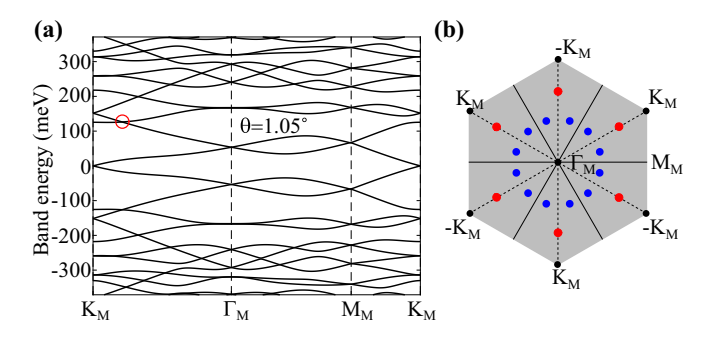


FIG. 6. Perfect metal phase of twisted bilayer graphene in the second chiral limit ($w_1 = 0$). (a) The band structure at $\theta = 1.05^{\circ}$ with the parameters $v_F = 5.944$ eV Å, |K| = 1.703 Å⁻¹, $w_1 = 0$, $w_0 = 77$ meV. (b) The Brillouin zone of the twisted bilayer graphene. The solid black lines represent the C_{2x} axis and its conjugations under C_{3z} ; the dashed black lines represent the effective mirror symmetry $M_x = C_{2x}I$ and its conjugations under C_{3z} . The red dots represent Dirac points in the mirror lines. The blue dots represent Dirac points at generic momenta.

at this momentum must form eigenstates of I. Suppose $|u\rangle$ is such an eigenstate with I eigenvalue 1, then we can show that $C_{2z}T|u\rangle$ must have the opposite I eigenvalue -1 due to the anticommutation between $C_{2z}T$ and I. Therefore $|u\rangle$ and $C_{2z}T|u\rangle$ form a doublet that has opposite I eigenvalues. This explains the double degeneracies at Γ_M and M_M shown in Fig. 6(a).

Next we prove that, for arbitrary even M, the Mth positive band is connected to the (M+1)th positive bands through 4l + 2 ($l \in \mathbb{N}$) Dirac points. (For odd M, we know by counting—see Fig. 6—that the Mth band is connected to the (M+1)th band through the double degeneracies at the *I*-invariant momenta). We only need to prove for the situation where the four bands $\epsilon_{M-1}(\mathbf{k})$, $\epsilon_{M}(\mathbf{k})$, $\epsilon_{M+1}(\mathbf{k})$, and $\epsilon_{M+2}(\mathbf{k})$ do not form fourfold degeneracies at high-symmetry momenta since otherwise $\epsilon_M(\mathbf{k})$ is already connected to $\epsilon_{M+1}(\mathbf{k})$. [As shown in Fig. 6(a), we also do not observe fourfold degeneracies at high-symmetry momenta]. We assume there are in total n_D Dirac points between the first M positive bands $\epsilon_1(\mathbf{k})\cdots\epsilon_M(\mathbf{k})$ and the other bands. The n_D Dirac points can appear above the Mth band, i.e., between $\epsilon_M(\mathbf{k})$ and $\epsilon_{M+1}(\mathbf{k})$, or below the first band, i.e., between $\epsilon_1(\mathbf{k})$ and $\epsilon_{-1}(\mathbf{k})$. According to the I symmetry, half of the BZ (\mathcal{B}) must have $n_D/2$ Dirac points. (The choice of \mathcal{B} is not unique. An example is shown in Fig. 4). With the $C_{2z}T$ symmetry, the number of Dirac points in \mathcal{B} is related to the Berry's phase surrounding B as [130]

$$\frac{n_D}{2} = \frac{1}{\pi} \oint_{\partial \mathcal{B}} d\mathbf{k} \cdot \mathbf{A}'(\mathbf{k}) \mod 2, \tag{36}$$

where $\mathbf{A}'(\mathbf{k}) = \sum_{n=1}^{M} i \langle u_n(\mathbf{k}) | \partial_{\mathbf{k}} u_n(\mathbf{k}) \rangle$ is Berry's connection of the first M positive bands. In the presence of the effective inversion symmetry I, the right-hand side of the above equation is determined by the I eigenvalues as [127,135-137]

$$\exp\left(i\oint_{\partial\mathcal{B}}d\mathbf{k}\cdot\mathbf{A}'(\mathbf{k})\right) = \prod_{\mathcal{K}}\prod_{n=1}^{M}\xi_{\mathcal{K},n},\tag{37}$$

where K indexes the four *I*-invariant momenta, and $\xi_{K,n}$ is the *I* eigenvalue of the *n*th positive band at the momentum K.

As discussed in the last paragraph, each doublet at an Iinvariant momentum has opposite I eigenvalues. Thus, there are an equal number of I eigenvalues 1 and -1 at the Iinvariant momenta; since the total number of states at the four I-invariant momenta is 4M, there are 2M eigenvalues with I = +1 and 2M eigenvalues with I = -1. Hence the righthand side of Eq. (37) is 1 and we have $\oint_{\partial \mathcal{B}} d\mathbf{k} \cdot \mathbf{A}'(\mathbf{k}) = 0$ mod 2π . According to Eq. (36), the total number of Dirac points is a multiple of 4, i.e., $n_D = 0 \mod 4$. As we have proved in Sec. IV, there must be 4l' + 2 ($l' \in \mathbb{N}$) Dirac points between $\epsilon_1(\mathbf{k})$ and $\epsilon_{-1}(\mathbf{k})$, then the number of Dirac points between $\epsilon_M(\mathbf{k})$ and $\epsilon_{M+1}(\mathbf{k})$ is $n_D - 4l' - 2 = 4l + 2$ with $l = n_D/4 - l' - 1 \in \mathbb{N}$. Thus the Mth positive band is always connected to the (M+1)th positive band through 4l+2Dirac points. According to the particle-hole symmetry P, the Mth negative band is also connected to the (M + 1)th negative band through 4l + 2 Dirac points. Therefore, the whole set of bands in the system will be connected.

In general, the 4l + 2 Dirac points between the Mth band the (M + 1)th band can be located anywhere in the BZ. However, with the C_{3z} and the C_{2x} symmetries of TBG, at least some of the 4l + 2 Dirac points must locate at the highsymmetry point or along high-symmetry lines of the BZ. We prove this statement by contradiction. The unitary point group of TBG is generated by C_{3z} , C_{2x} , and the effective inversion I and hence is isomorphic to the point group D_{3d} , which has 12 elements in total. If all the Dirac points between the Mth band the (M + 1)th band are located at generic momenta, then the number of Dirac points would be a multiple of 12, as represented by the blue dots in Fig. 6(b), leading to a contradiction with the 4l + 2 Dirac points. Therefore, there must be two (modulo 4) Dirac points at the high-symmetry points or along the high-symmetry lines. As a consequence, the entire set of bands of TBG in the second chiral limit must be connected along the high-symmetry lines. For example, as shown in Fig. 6(a), there is a crossing between the second and third bands in the high-symmetry line $\Gamma_M - K_M$. (This crossing is protected by the effective mirror symmetry $M_x = C_{2x}I$). Under the actions of C_{2x} and C_{3z} , there are in total six symmetry counterparts of this crossing point (including itself). Thus the number of Dirac points is consistent with 4l + 2 with l = 1.

VII. CONCLUSIONS

In this paper, we showed that even the simple, well-studied BM TBG model still has several surprises related to the deep physics that it describes. We have proved that the band structure in a single graphene valley of TBG is anomalous, i.e., does not have lattice support that respects the $C_{2z}T$ and \mathcal{P} symmetries. The anomaly manifests as (i) a \mathbb{Z}_2 nontrivial topology protected \mathcal{P} of the 2M bands $\epsilon_{-M}(\mathbf{k}) \cdots \epsilon_{M}(\mathbf{k})$ for arbitrary M, provided that the 2M bands are gapped from other bands, and (ii) 4l + 2 ($l \in \mathbb{N}$) Dirac points between $\epsilon_{-1}(\mathbf{k})$ and $\epsilon_{1}(\mathbf{k})$. In the second chiral limit ($w_{1} = 0$), the anomaly manifests as (iii) a perfect metal phase where all the bands are connected.

As a consequence of the symmetry anomaly, a faithful description of TBG that respects all the symmetries of TBG, including \mathcal{P} , is forced to adopt a momentum space formalism. Any tight-binding description [19,52,53,55,65] of TBG with

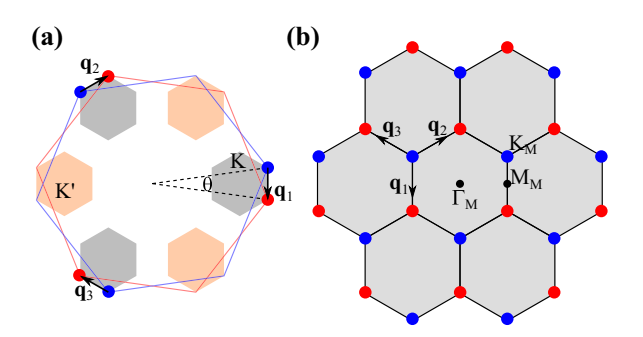


FIG. 7. The **Q** lattice for the momentum space Hamiltonian of twisted bilayer graphene. (a) The blue and red hexagons represent the Brillouin zones of the top layer and the bottom layer, respectively. The blue and red dots represent the positions of Dirac points of the two layers in the graphene valley K, respectively. (b) The **Q** lattice formed by adding $\mathbf{q}_{1,2,3}$ iteratively. At each blue dot a plane-wave state from the top layer is assigned, and at each red dot a plane-wave state from the bottom layer is assigned.

a finite number of orbitals must break at least one of the $C_{2z}T$ and \mathcal{P} symmetries (or the valley symmetry if the tight-binding model mixes the two graphene valleys of TBG). In the other works of our series on TBG [109–113], the interacting physics is studied using a momentum space formalism.

ACKNOWLEDGMENTS

We thank Aditya Cowsik and Fang Xie for valuable discussions. This work was supported by US Department of Energy Grant No. DE-SC0016239, the Schmidt Fund for Innovative Research, Simons Investigator Grant No. 404513, the Packard Foundation, the Gordon and Betty Moore Foundation through Grant No. GBMF8685 towards the Princeton theory program, and a Guggenheim Fellowship from the John Simon Guggenheim Memorial Foundation. Further support was provided by NSF-EAGER Grant No. DMR 1643312, NSF-MRSEC Grants No. DMR-1420541 and No. DMR-2011750, ONR Grant No. N00014-20-1-2303, the Gordon and Betty Moore Foundation through Grant No. GBMF8685 towards the Princeton theory program, BSF Israel US Foundation Grant No. 2018226, and the Princeton Global Network Funds.

APPENDIX A: HAMILTONIAN OF TWISTED BILAYER GRAPHENE IN MOMENTUM SPACE

1. The Hamiltonian

Here we briefly introduce the momentum space Hamiltonian $H(\mathbf{k})$ corresponding to Eq. (1). Readers may refer to the supplementary materials of Ref. [56] for more details. The basis of $H(\mathbf{k})$ is $|\phi_{\mathbf{Q},\alpha}(\mathbf{k})\rangle$, where \mathbf{k} is a momentum in the moiré BZ, \mathbf{Q} is a point in the lattice shown in Fig. 7, and $\alpha=1,2$ is the sublattice index of graphene. There are two types of \mathbf{Q} lattices: the blue lattice \mathcal{Q}_T and the red lattice \mathcal{Q}_B . For $\mathbf{Q} \in \mathcal{Q}_T$, the basis $|\phi_{\mathbf{Q},\alpha}(\mathbf{k})\rangle$ is a plane-wave state from the top layer

$$|\phi_{\mathbf{Q},\alpha}(\mathbf{k})\rangle = \frac{1}{\sqrt{N}} \sum_{\mathbf{R}} e^{i(\mathbf{R} + t_{\alpha}) \cdot (\mathbf{k} - \mathbf{Q})} |\mathbf{R} + t_{\alpha}\rangle,$$
 (A1)

where N is the number of lattices in the top layer graphene, \mathbf{R} indexes all the lattices of the top layer graphene, t_{α} is the sublattice vector of the top layer graphene, and $|\mathbf{R} + t_{\alpha}\rangle$ is the atomic orbital at $\mathbf{R} + t_{\alpha}$. For $\mathbf{Q} \in \mathcal{Q}_B$, the basis $|\phi_{\mathbf{Q},\alpha}(\mathbf{k})\rangle$ is a plane-wave state from the bottom layer:

$$|\phi_{\mathbf{Q},\alpha}(\mathbf{k})\rangle = \frac{1}{\sqrt{N}} \sum_{\mathbf{R}'} e^{i(\mathbf{R}' + t'_{\alpha}) \cdot (\mathbf{k} - \mathbf{Q})} |\mathbf{R}' + t'_{\alpha}\rangle,$$
 (A2)

where N is the number of lattices in the bottom layer graphene (same as the one in the top layer), \mathbf{R}' indexes all the lattices of the bottom layer graphene, t_{α}' is the sublattice vector of the top layer graphene, and $|\mathbf{R}' + t_{\alpha}'\rangle$ is the atomic orbital at $\mathbf{R}' + t_{\alpha}'$. The Hamiltonian [Eq. (1)] on the basis $|\phi_{\mathbf{Q},\alpha}(\mathbf{k})\rangle$ is given by

$$H_{\mathbf{Q},\mathbf{Q}'}(\mathbf{k}) = v_F \delta_{\mathbf{Q},\mathbf{Q}'}(\mathbf{k} - \mathbf{Q}) \cdot \boldsymbol{\sigma} - \frac{\theta}{2} \zeta_{\mathbf{Q}} \delta_{\mathbf{Q},\mathbf{Q}'}(\mathbf{k} - \mathbf{Q}) \times \boldsymbol{\sigma} + \sum_{i=1}^{3} \left(\delta_{\mathbf{Q}' - \mathbf{Q},\mathbf{q}_j} + \delta_{\mathbf{Q} - \mathbf{Q}',\mathbf{q}_j} \right) T_j, \tag{A3}$$

where $\sigma = (\sigma_x, \sigma_y)$ and T_j (j = 1, 2, 3) are 2×2 matrices in the sublattice space, $\zeta_{\mathbf{Q}} = 1$ for $\mathbf{Q} \in \mathcal{Q}_T$, and $\zeta_{\mathbf{Q}} = -1$ for $\mathbf{Q} \in \mathcal{Q}_B$.

2. The periodicity of Bloch states

An eigenstate of Eq. (1) at a given momentum \mathbf{k} can be written as a linear combination of the Bloch basis as $|\psi_n(\mathbf{k})\rangle = \sum_{\mathbf{Q},\alpha} |\phi_{\mathbf{Q},\alpha}(\mathbf{k})\rangle u_{\mathbf{Q}\alpha,n}(\mathbf{k})$. Here n is the band index. It should be noticed that the basis states in Eqs. (A1) and (A2) are *not* periodic in the moiré BZ since $|\phi_{\mathbf{Q},\alpha}(\mathbf{k}+\mathbf{G})\rangle = |\psi_{\mathbf{Q}-\mathbf{G},\alpha}(\mathbf{k})\rangle$ by definition. In order for the Bloch state $|\psi_n(\mathbf{k})\rangle$ to be periodic in the moiré BZ, i.e., $|\psi_n(\mathbf{k}+\mathbf{G})\rangle = |\psi_n(\mathbf{k})\rangle$, $u_{\mathbf{Q},\alpha}(\mathbf{k})$ should satisfy $u_{\mathbf{Q},\alpha}(\mathbf{k}+\mathbf{G}) = u_{\mathbf{Q}-\mathbf{G},\alpha}(\mathbf{k})$. We introduce the embedding matrix

$$V_{\mathbf{Q},\mathbf{Q}'}^{\mathbf{G}} = \delta_{\mathbf{Q}-\mathbf{G},\mathbf{Q}'} \tag{A4}$$

such that we can write the periodicity of Bloch states as

$$|u_n(\mathbf{k} + \mathbf{G})\rangle = V^{\mathbf{G}}|u_n(\mathbf{k})\rangle,$$
 (A5)

where $|u_n(\mathbf{k})\rangle = (u_{\mathbf{Q}_1,1,n}(\mathbf{k}), u_{\mathbf{Q}_1,2,n}(\mathbf{k}), u_{\mathbf{Q}_2,1,n}(\mathbf{k}) \cdots)^T$. While exact Bloch periodicity requires that the cutoff in the lattice \mathbf{Q} be large, we have showed—around the first magic angle [109]—that we can obtain machine precision accuracy in the first moiré BZ by taking a small cutoff in \mathbf{Q} .

3. Symmetry operators in the momentum space

The crystalline symmetry group of the single valley Hamiltonian is the magnetic space group P6'2'2 (no. 177.151 in the BNS setting [123]). The generators of this group are the C_{3z} symmetry

$$H(C_{3z}\mathbf{k}) = D(C_{3z})H(C_{3z}\mathbf{k})D^{\dagger}(C_{3z}) \tag{A6}$$

where $D_{\mathbf{Q}',\mathbf{Q}}(C_{3z}) = e^{i\frac{2\pi}{3}\sigma_z}\delta_{\mathbf{Q}',C_{3z}\mathbf{Q}}$, the C_{2x} symmetry

$$H(C_{2x}\mathbf{k}) = D(C_{2x})H(C_{2x}\mathbf{k})D^{\dagger}(C_{2x}) \tag{A7}$$

where $D_{\mathbf{Q}',\mathbf{Q}}(C_{2x}) = \sigma_x \delta_{\mathbf{Q}',C_{2x}\mathbf{Q}}$ and $C_{2x}\mathbf{q}_1 = -\mathbf{q}_1$, and the $C_{2z}T$ symmetry

$$H(\mathbf{k}) = D(C_{2z}T)H_{\mathbf{O},\mathbf{O}}^*(\mathbf{k})D^T(C_{2z}T)$$
 (A8)

where $D_{\mathbf{O}',\mathbf{O}}(C_{2z}T) = \sigma_x \delta_{\mathbf{O}',\mathbf{O}}$. It should be noticed that all rotations of momenta here are with respect to the Γ_M point of the moiré BZ.

When the second term in Eq. (A3) is negligible, $H(\mathbf{k})$ has an emergent unitary particle-hole symmetry

$$H(-\mathbf{k}) = -D(P)H(\mathbf{k})D^{\dagger}(P) \tag{A9}$$

where $D_{\mathbf{Q}',\mathbf{Q}}(P) = \delta_{\mathbf{Q}',-\mathbf{Q}}\zeta_{\mathbf{Q}}$, and $\zeta_{\mathbf{Q}} = 1$ for $\mathbf{Q} \in \mathcal{Q}_T$ and $\zeta_{\mathbf{Q}} = -1$ for $\mathbf{Q} \in \mathcal{Q}_B$. The antiunitary particle-hole symmetry $\mathcal{P} = PC_{2z}T$ in momentum space is

$$H(-\mathbf{k}) = -D(\mathcal{P})H^*(-\mathbf{k})D^T(\mathcal{P}), \tag{A10}$$

where $D_{\mathbf{Q},\mathbf{Q}'}(\mathcal{P}) = \sigma_x \delta_{\mathbf{Q}',-\mathbf{Q}} \zeta_{\mathbf{Q}}$. When $w_0 = 0$, $H(\mathbf{k})$ has an emergent chiral symmetry

$$H(\mathbf{k}) = -D^{\dagger}(C)H(\mathbf{k})D(C), \tag{A11}$$

where $D_{\mathbf{Q},\mathbf{Q}'}(C) = \sigma_z \delta_{\mathbf{Q},\mathbf{Q}'}$. When $w_1 = 0$, $H(\mathbf{k})$ has an another emergent chiral symmetry (the second chiral symmetry)

$$H(\mathbf{k}) = -D^{\dagger}(C')H(\mathbf{k})D(C'), \tag{A12}$$

where $D_{\mathbf{Q},\mathbf{Q}'}(C') = \sigma_z \delta_{\mathbf{Q},\mathbf{Q}'} \zeta_{\mathbf{Q}}$. The embedding matrix transforms under the unitary operators $(g = C_{3z}, C_{2x}, P, C, C')$ as

$$D(g)V^{\mathbf{G}}D^{\dagger}(g) = V^{g\mathbf{G}}.$$
 (A13)

For the unitary operator $C_{2z}T$, we have

$$D(C_{2z}T)V^{G*}D^{T}(C_{2z}T) = V^{G}.$$
 (A14)

One can verify the two identities by explicitly acting the symmetry operators on the embedding matrix.

4. The sewing matrices of symmetry operators

For the unitary crystalline symmetries, e.g., $g = C_{3z}$, C_{2x} , P, C, C', we define the sewing matrices as

$$B_{n'n}^{(g)}(\mathbf{k}) = \langle u_{n'}(g\mathbf{k})|D(g)|u_n(\mathbf{k})\rangle. \tag{A15}$$

For the antiunitary symmetries, e.g., $g = C_{2z}T$, \mathcal{P} , we define the sewing matrices as

$$B_{n'n}^{(g)}(\mathbf{k}) = \langle u_{n'}(g\mathbf{k})|D(g)|u_n^*(\mathbf{k})\rangle. \tag{A16}$$

Using the identities Eqs. (A13) and (A14), we obtain that the sewing matrices are periodic in momentum space, i.e., $B^{(g)}(\mathbf{k} + \mathbf{G}) = B^{(g)}(\mathbf{k})$ for arbitrary reciprocal lattice **G**. The explicit expressions for the sewing matrices depend on different bases, and will be given in Ref. [110] for the cases needed for our interacting problem.

APPENDIX B: MORE DISCUSSIONS ON THE PARTICLE-HOLE SYMMETRY

1. 1. Effect of in-plane lattice relaxation

We first show that the in-plane relaxation does not directly lead to the particle-hole symmetry breaking. In Ref. [138], Koshino et al. obtained the relaxed lattice structure of TBG by minimizing the elastic energy. The in-plane displacement of atoms in the two layers can be approximated as

$$\mathbf{s}^{(l)}(\mathbf{r}) = \begin{cases} \mathbf{s}(\mathbf{r}), & l = T \\ -\mathbf{s}(\mathbf{r}), & l = B \end{cases}$$
(B1)

where l is the layer index and

$$\mathbf{s}(\mathbf{r}) = \frac{i}{2} \sum_{\mathbf{G}} \mathbf{s}_{\mathbf{G}} e^{i\mathbf{G} \cdot \mathbf{r}}.$$
 (B2)

 $\mathbf{s}_{\mathbf{G}}$ is an odd function of \mathbf{G} and is dominated by the components on the shortest G vectors [139]. For example, for $|\mathbf{G}| = |\mathbf{b}_{M,1}|$, $\mathbf{s}_{\mathbf{G}}$ takes the form [139]

$$\mathbf{s}_{\mathbf{G}} = \frac{s_0}{|\mathbf{b}_{M1}|} (-G_{y}, G_{x}), \qquad (|\mathbf{G}| = |\mathbf{b}_{M1}|),$$
 (B3)

where s_0 is the length of the displacement vectors. The inplane displacement leads to two new terms in the Hamiltonian of TBG: (i) the correction of the intralayer hopping, which has a form of pseudovector potential, and (ii) the correction to the interlayer hopping. The pseudovector potential has the form A:

$$\mathbf{A}_{x}(\mathbf{r}) = \gamma [s_{xx}(\mathbf{r}) - s_{yy}(\mathbf{r})], \quad \mathbf{A}_{y}(\mathbf{r}) = -2\gamma s_{xy}(\mathbf{r})$$
 (B4)

with $s_{ij} = \frac{1}{2}(\partial_i v_j + \partial_j v_i)$ being the strain tensor and γ the coupling constant. Since s_G is real and odd in G, A(r) is real and even in **r**. The pseudovector potential enters the TBG Hamiltonian as

$$-iv_F \partial_{\mathbf{r}} \cdot \mathbf{\sigma} \rightarrow v_F (-i\partial_{\mathbf{r}} + A(\mathbf{r})\tau_z) \cdot \mathbf{\sigma}.$$
 (B5)

The τ_z factor in the pseudovector potential term comes from the fact that $\mathbf{s}^{(T)} = -\mathbf{s}^{(B)} = \mathbf{s}(\mathbf{r})$ [Eq. (B1)]. We find that the pseudovector potential term respects all the symmetries. In particular, it respects the $C_{2z}T = \sigma_x K$ and the $\mathcal{P} = i\tau_y \sigma_x K$ symmetries, which protect the stable topology.

With the in-plane displacement fields, the interlayer coupling changes to [139]

$$T(\mathbf{r}) \to \tilde{T}(\mathbf{r}) = \sum_{i=1}^{3} e^{-i\mathbf{K}_{i} \cdot \mathbf{s}(\mathbf{r}) - i\mathbf{q}_{i} \cdot \mathbf{r}} \cdot T_{i},$$
 (B6)

where \mathbf{K}_1 is the \mathbf{K} vector shown in Fig. 7, $\mathbf{K}_2 = C_{3z}\mathbf{K}_1$, $\mathbf{K_3} = C_{3z}\mathbf{K_2}$, and T_i are given in Eq. (3). The corresponding Hamiltonian matrix can be written as

$$\begin{pmatrix} 0 & \tilde{T}(\mathbf{r}) \\ \tilde{T}^{\dagger}(\mathbf{r}) & 0 \end{pmatrix} = \sum_{i} [f_{i}(\mathbf{r})\tau_{x} \otimes T_{i} + g_{i}(\mathbf{r})\tau_{y} \otimes T_{i}], \quad (B7)$$

with $f_i(\mathbf{r})$ and $g_i(\mathbf{r})$ being the real part and imaginary part of $e^{-i\mathbf{K}_i \cdot \mathbf{s}(\mathbf{r}) - i\mathbf{q}_i \cdot \mathbf{r}}$, respectively. Since $s(\mathbf{r})$ is odd in \mathbf{r} , there is $f_i(\mathbf{r}) = f_i(-\mathbf{r})$ and $g_i(\mathbf{r}) = -g_i(\mathbf{r})$. One can find that the interlayer coupling respects both $C_{2z}T = \sigma_x K$ and $\mathcal{P} = i\tau_y \sigma_x K$.

Therefore, the in-plane relaxation does not directly lead to particle-hole symmetry breaking. This is also numerically shown in Refs. [139,140].

2. k dependence in the interlayer hopping

The continuous models of TBG discussed in the rest of this paper have made an approximation on the interlayer coupling: We have neglected the k dependence of the Fourier transformation of the interlayer hopping. References [139,140] have shown that keeping the k dependence in $t(\mathbf{q})$ will lead to a particle-hole asymmetry in the energy spectrum. Reference [140] shows that keeping linear order of k in the k dependence is a good approximation. Here we derive the linear k dependence explicitly. Following Eq. (14) of the supplementary

material of Ref. [56], we have the intervalley coupling on the basis of Eqs. (A1) and (A2):

$$H_{\mathbf{Q},\mathbf{Q}'}(\mathbf{k}) = \sum_{j=1}^{3} t_{\mathbf{K}_{j}+\mathbf{k}-\mathbf{Q}} \delta_{\mathbf{Q},\mathbf{Q}'-\mathbf{q}_{j}} \cdot \bar{T}_{j} \quad (\mathbf{Q} \in \mathcal{Q}_{T}, \mathbf{Q}' \in \mathcal{Q}_{B})$$
(B8)

where $t_{\mathbf{q}} = t_0 \exp[-\alpha(|\mathbf{q}|d_{\perp})^{\gamma}]$ is the Fourier transformation of the interlayer coupling with d_{\perp} being the distance between the two layers, and

$$\bar{T}_i = \sigma_0 + \left[\sigma_x \cos \frac{2\pi (i-1)}{3} + \sigma_y \sin \frac{2\pi (i-1)}{3} \right].$$
 (B9)

Here \mathbf{K}_1 is the \mathbf{K} vector shown in Fig. 7, $\mathbf{K}_2 = C_{3z}\mathbf{K}_1$, and $\mathbf{K}_3 = C_{3z}\mathbf{K}_2$. The parameters in $t_{\mathbf{q}}$ have been fitted as $\alpha = 0.13$, $\gamma = 1.25$. For simplicity here we assume d_{\perp} is uniform in real space.

We expand $t_{\mathbf{K}_i+\mathbf{k}-\mathbf{Q}}$ to leading order of $\mathbf{k}-\mathbf{Q}$ as

$$t_{\mathbf{K}_j + \mathbf{k} - \mathbf{Q}} \approx t_{\mathbf{K}_j} \left(1 - \alpha \gamma (d_{\perp} | \mathbf{K}_j |)^{\gamma} \frac{\mathbf{K}_j \cdot (\mathbf{k} - \mathbf{Q})}{|\mathbf{K}_j|^2} \right).$$
 (B10)

Then we obtain the correction to the continuous model as

$$\delta H_{\mathbf{Q},\mathbf{Q}'}(\mathbf{k}) = -\lambda \sum_{j=1}^{3} \delta_{\mathbf{Q},\mathbf{Q}'-\mathbf{q}_{j}} \cdot \frac{\mathbf{K}_{j} \cdot (\mathbf{k} - \mathbf{Q})}{|\mathbf{K}_{j}|^{2}} \cdot \bar{T}_{j} \quad (B11)$$

for $\mathbf{Q} \in \mathcal{Q}_T$, $\mathbf{Q}' \in \mathcal{Q}_B$, and

$$\delta H_{\mathbf{Q},\mathbf{Q}'}(\mathbf{k}) = -\lambda \sum_{j=1}^{3} \delta_{\mathbf{Q},\mathbf{Q}'+\mathbf{q}_{j}} \cdot \frac{\mathbf{K}_{j} \cdot (\mathbf{k} - \mathbf{Q}')}{|\mathbf{K}_{j}|^{2}} \cdot \bar{T}_{j} \quad (B12)$$

for $\mathbf{Q} \in \mathcal{Q}_B$, $\mathbf{Q}' \in \mathcal{Q}_T$. Here $\lambda = t_{\mathbf{K}} \alpha \gamma (d_{\perp} |\mathbf{K}|)^{\gamma}$. Since $\delta H_{\mathbf{Q},\mathbf{Q}'}(\mathbf{k})$ still consists of σ_0 , σ_x , σ_y , it respects the $C_{2z}T$ symmetry. However, it breaks the unitary particle-hole symmetry P [Eq. (4)] and hence the antiunitary particle-hole symmetry $\mathcal{P} = P \cdot C_{2z}T$. We use the parameter $\lambda = 180 \text{ meV}$ to make a significant particle-hole asymmetry in the band structure: the lower band at Γ_M has the energy -1.34 meV and the upper band has the energy 5.16 meV (Fig. 8). However, we find the error of the particle-hole symmetry for the Bloch wave functions [Eq. (9)] as $error(\mathcal{P}) = 0.07$, which is still weak. A more realistic model should include both the in-plane relaxation and the k dependence of the interlayer hopping [139,140]. As discussed in the last subsection, without the k dependence, the in-plane relaxation will not lead to \mathcal{P} breaking. Hence we claim that the error of the \mathcal{P} symmetry in this more realistic model will have the same order as 0.13.

APPENDIX C: THE GAUGE OF CHERN BAND BASIS

In Sec. V we have explained that the choice of Chern band basis due to the $C_{2z}T$ gauge fixing [Eq. (26)] has two ambiguities: (i) the choice of the two branches of $\frac{\theta_n(\mathbf{k})}{2}$, i.e., $\frac{\theta_n(\mathbf{k})}{2}$ and $\frac{\theta_n(\mathbf{k})}{2} + \pi$, and (ii) the choice of $|u_1(\mathbf{k})\rangle$ and $|u_{-1}(\mathbf{k})\rangle$ at Dirac points where the two bands are degenerate. Both ambiguities lead to an ambiguity when choosing $|v_{\pm}(\mathbf{k})\rangle$. If we replace $\frac{\theta_1(\mathbf{k})}{2}$ by $\frac{\theta_1(\mathbf{k})}{2} + \pi$ in Eq. (26), then the two Chern band states in the new gauge $|v'_{+}(\mathbf{k})\rangle$ are related to the Chern

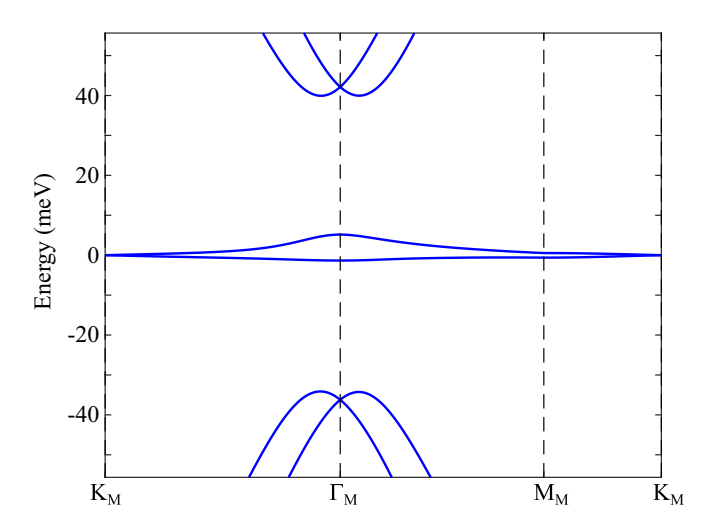


FIG. 8. Significant particle-hole asymmetry in the energy spectrum when the **k** dependence of the interlayer coupling is considered. The parameters used in the Hamiltonian are $v_F = 5.944$ eV Å, $|K| = 1.703 \text{ Å}^{-1}$, $w_1 = 110 \text{ meV}$, $w_0 = 0.7w_1$, $\lambda = 250 \text{ meV}$, $\theta = 1.05^{\circ}$.

band states in the previous gauge as

$$|v'_{\pm}(\mathbf{k})\rangle = \frac{1}{\sqrt{2}} \left[-e^{i\frac{\theta_{1}(\mathbf{k})}{2}} |u_{1}(\mathbf{k})\rangle \pm ie^{i\frac{\theta_{-1}(\mathbf{k})}{2}} |u_{-1}(\mathbf{k})\rangle \right]$$
$$= -|v_{\pm}(\mathbf{k})\rangle. \tag{C1}$$

Therefore, changing the branch of $\frac{\theta_1(\mathbf{k})}{2}$ at \mathbf{k} will interchange the two states $|v_{\pm}(\mathbf{k})\rangle$ at \mathbf{k} . One can show that changing the branch of $\frac{\theta_{-1}(\mathbf{k})}{2}$ will also interchange the two states $|v_{\pm}(\mathbf{k})\rangle$ for the same reason. We then consider interchanging $|u_{\pm 1}(\mathbf{k})\rangle$ at a Dirac point \mathbf{k}_D . The Chern band states $|v''_{\pm}(\mathbf{k}_D)\rangle$ defined with the interchanged $|u_{\pm 1}(\mathbf{k}_D)\rangle$ become

$$|v''_{\pm}(\mathbf{k}_D)\rangle = \frac{1}{\sqrt{2}} \left[e^{i\frac{\theta_{-1}(\mathbf{k}_D)}{2}} |u_{-1}(\mathbf{k}_D)\rangle \pm i e^{i\frac{\theta_{1}(\mathbf{k}_D)}{2}} |u_{1}(\mathbf{k}_D)\rangle \right]$$
$$= \pm i |v_{\pm}(\mathbf{k})\rangle. \tag{C2}$$

Thus interchanging $|u_{\pm 1}(\mathbf{k})\rangle$ at Dirac points will interchange $|v_{\pm}(\mathbf{k})\rangle$ at the Dirac points.

Due to the ambiguities discussed above, at each **k** point we only have two choices for $|v_{\pm}(\mathbf{k})\rangle$ (up to phase factors). Starting with $|v_{\pm}(\mathbf{k}_0)\rangle$ at a given momentum \mathbf{k}_0 , the condition Eq. (27) will uniquely determine the two branches of $|v_{\pm}(\mathbf{k})\rangle$ over the whole BZ. To be specific, we consider the choice of $|v_{\pm}(\mathbf{k}_0+\mathbf{q})\rangle$ for **q** being a small momentum. Suppose $|v'_{\pm}(\mathbf{k}_0+\mathbf{q})\rangle$ is returned by Eq. (26) without considering Eq. (27). Then if they satisfy $|\langle v_m(\mathbf{k}_0)|v'_{m'}(\mathbf{k}_0+\mathbf{q})\rangle| \approx \delta_{mm'}$, we choose $|v_{\pm}(\mathbf{k}_0+\mathbf{q})\rangle = |v'_{\pm}(\mathbf{k}_0+\mathbf{q})\rangle$; otherwise, i.e., $|\langle v_m(\mathbf{k}_0)|v'_{m'}(\mathbf{k}_0+\mathbf{q})\rangle| \approx 1 - \delta_{mm'}$, we choose $|v_{\pm}(\mathbf{k}_0+\mathbf{q})\rangle = |v'_{\pm}(\mathbf{k}_0+\mathbf{q})\rangle$. Repeating this procedure over the whole BZ iteratively will uniquely determine the two branches of $|v_{\pm}(\mathbf{k})\rangle$.

We now explain that the obtained two branches by the method introduced above must be Chern bands. We first consider **k** not at the Dirac points. Due to the discussion in Sec. V, if a smooth branch of $\frac{\theta_n(\mathbf{k})}{2}$ is chosen, the states

 $|v_{\pm}(\mathbf{k})\rangle$ will have smooth Berry's curvatures $\pm f(\mathbf{k})$. On the other hand, if the branch of $\frac{\theta_n(\mathbf{k})}{2}$ changes at \mathbf{k}_{\star} , then there is $\lim_{\mathbf{q}\to 0}|\langle v_+(\mathbf{k}_{\star})|v_+(\mathbf{k}_{\star}+\mathbf{q})\rangle|=|\langle v_+(\mathbf{k}_{\star})|v_-(\mathbf{k}_{\star})\rangle|=0$ and hence the Berry's curvatures of $|v_{\pm}(\mathbf{k})\rangle$ will be discontinuous at \mathbf{k}_{\star} . Therefore, choosing a smooth branch of $\frac{\theta_n(\mathbf{k})}{2}$ is equivalent to choosing $|v_{\pm}(\mathbf{k})\rangle$ such that they have continuous Berry curvatures. Thus Eq. (27), which guarantees continuous Berry curvatures, also enforces that $|v_{\pm}(\mathbf{k})\rangle$ must have Berry's curvatures $\pm f(\mathbf{k})$. We then consider the Dirac points. Since there is a finite number of Dirac points in the BZ, the integral of Berry's curvature in the (infinite small) neighborhoods of the Dirac points approaches zero as long as Eq. (27) holds such that Berry's curvature is nondivergent. Therefore, the integrals of Berry's curvatures of $|v_{\pm}(\mathbf{k})\rangle$ subject to the condition Eq. (27) are $\pm \frac{1}{2\pi} \int d^2\mathbf{k} f(\mathbf{k}) = \pm e_2$.

Now we explicitly show why Berry's curvatures of Eq. (26) are not divergent at the Dirac points if Eq. (27) holds. We consider a linearized $k \cdot p$ model around a single Dirac point $H = k_x \sigma_x + k_y \sigma_y$, where the $C_{2z}T$ operator is $\sigma_x K$. Since Berry's curvature is gauge invariant, we take the particular gauge $\theta_1(\mathbf{k}) = \theta_{-1}(\mathbf{k}) = 0$ in the calculation. The Bloch states in this gauge are

$$|u_1(\mathbf{k})\rangle = \frac{1}{\sqrt{2}} \begin{pmatrix} e^{-i\frac{\phi(\mathbf{k})}{2}} \\ e^{i\frac{\phi(\mathbf{k})}{2}} \end{pmatrix}, \quad |u_{-1}(\mathbf{k})\rangle = \frac{1}{\sqrt{2}} \begin{pmatrix} -ie^{-i\frac{\phi(\mathbf{k})}{2}} \\ ie^{i\frac{\phi(\mathbf{k})}{2}} \end{pmatrix}, \tag{C3}$$

where $\phi(\mathbf{k}) = \arccos \frac{k_x}{\sqrt{k_x^2 + k_y^2}}$. Then the recombined Chern bases are $|v_+(\mathbf{k})\rangle = (e^{-i\frac{\phi(\mathbf{k})}{2}}, 0)^T$, $|v_-(\mathbf{k})\rangle = (0, e^{i\frac{\phi(\mathbf{k})}{2}})^T$. They satisfy Eq. (27) and have vanishing Berry curvatures in the neighbourhood of the Dirac point.

- R. Bistritzer and A. H. MacDonald, Moiré bands in twisted double-layer graphene, Proc. Natl. Acad. Sci. USA 108, 12233 (2011).
- [2] Y. Cao, V. Fatemi, A. Demir, S. Fang, S. L. Tomarken, J. Y. Luo, J. D. Sanchez-Yamagishi, K. Watanabe, T. Taniguchi, E. Kaxiras, R. C. Ashoori, and P. Jarillo-Herrero, Correlated insulator behaviour at half-filling in magic-angle graphene superlattices, Nature (London) 556, 80 (2018).
- [3] D. K. Efimkin and A. H. MacDonald, Helical network model for twisted bilayer graphene, Phys. Rev. B 98, 035404 (2018).
- [4] Y. Xie, B. Lian, B. Jäck, X. Liu, C.-L. Chiu, K. Watanabe, T. Taniguchi, B. A. Bernevig, and A. Yazdani, Spectroscopic signatures of many-body correlations in magic-angle twisted bilayer graphene, Nature (London) 572, 101 (2019).
- [5] I. Das, X. Lu, J. Herzog-Arbeitman, Z.-D. Song, K. Watanabe, T. Taniguchi, B. A. Bernevig, and D. K. Efetov, Symmetry broken Chern insulators and magic series of Rashba-like Landau level crossings in magic angle bilayer graphene, Nature Physics (2020), doi: 10.1038/s41567-021-01186-3.
- [6] H. C. Po, L. Zou, A. Vishwanath, and T. Senthil, Origin of Mott Insulating Behavior and Superconductivity in Twisted Bilayer Graphene, Phys. Rev. X 8, 031089 (2018).
- [7] J. F. Dodaro, S. A. Kivelson, Y. Schattner, X.-Q. Sun, and C. Wang, Phases of a phenomenological model of twisted bilayer graphene, Phys. Rev. B 98, 075154 (2018).
- [8] N. F. Q. Yuan and L. Fu, Model for the metal-insulator transition in graphene superlattices and beyond, Phys. Rev. B 98, 045103 (2018).
- [9] M. Ochi, M. Koshino, and K. Kuroki, Possible correlated insulating states in magic-angle twisted bilayer graphene under strongly competing interactions, Phys. Rev. B 98, 081102(R) (2018).
- [10] X. Y. Xu, K. T. Law, and P. A. Lee, Kekulé valence bond order in an extended Hubbard model on the honeycomb lattice with possible applications to twisted bilayer graphene, Phys. Rev. B 98, 121406(R) (2018).
- [11] J. W. F. Venderbos and R. M. Fernandes, Correlations and electronic order in a two-orbital honeycomb lattice model for twisted bilayer graphene, Phys. Rev. B **98**, 245103 (2018).
- [12] J. Kang and O. Vafek, Strong Coupling Phases of Partially Filled Twisted Bilayer Graphene Narrow Bands, Phys. Rev. Lett. 122, 246401 (2019).

- [13] J. Liu, Z. Ma, J. Gao, and X. Dai, Quantum Valley Hall Effect, Orbital Magnetism, and Anomalous Hall Effect in Twisted Multilayer Graphene Systems, Phys. Rev. X 9, 031021 (2019).
- [14] Y. Jiang, X. Lai, K. Watanabe, T. Taniguchi, K. Haule, J. Mao, and E. Y. Andrei, Charge order and broken rotational symmetry in magic-angle twisted bilayer graphene, Nature (London) 573, 91 (2019).
- [15] Y. Choi, J. Kemmer, Y. Peng, A. Thomson, H. Arora, R. Polski, Y. Zhang, H. Ren, J. Alicea, G. Refael *et al.*, Electronic correlations in twisted bilayer graphene near the magic angle, Nat. Phys. 15, 1174 (2019).
- [16] H. Polshyn, M. Yankowitz, S. Chen, Y. Zhang, K. Watanabe, T. Taniguchi, C. R. Dean, and A. F. Young, Large linear-intemperature resistivity in twisted bilayer graphene, Nat. Phys. 15, 1011 (2019).
- [17] J. H. Pixley and E. Y. Andrei, Ferromagnetism in magic-angle graphene, Science 365, 543 (2019).
- [18] M. Xie and A. H. MacDonald, Nature of the Correlated Insulator States in Twisted Bilayer Graphene, Phys. Rev. Lett. 124, 097601 (2020).
- [19] N. Bultinck, E. Khalaf, S. Liu, S. Chatterjee, A. Vishwanath, and M. P. Zaletel, Ground State and Hidden Symmetry of Magic-Angle Graphene at Even Integer Filling, Phys. Rev. X 10, 031034 (2020).
- [20] K. P. Nuckolls, M. Oh, D. Wong, B. Lian, K. Watanabe, T. Taniguchi, B. A. Bernevig, and A. Yazdani, Strongly correlated chern insulators in magic-angle twisted bilayer graphene, Nature 588, 610 (2020).
- [21] S. Wu, Z. Zhang, K. Watanabe, T. Taniguchi, and E. Y. Andrei, Chern insulators and topological flat-bands in magic-angle twisted bilayer graphene, Nat. Mat. 20, 488 (2021).
- [22] Y. Saito, J. Ge, L. Rademaker, K. Watanabe, T. Taniguchi, D. A. Abanin, and A. F. Young, Hofstadter subband ferromagnetism and symmetry broken chern insulators in twisted bilayer graphene, Nat. Phys. 17, 478 (2021).
- [23] D. Wong, K. P. Nuckolls, M. Oh, B. Lian, Y. Xie, S. Jeon, K. Watanabe, T. Taniguchi, B. A. Bernevig, and A. Yazdani, Cascade of electronic transitions in magic-angle twisted bilayer graphene, Nature (London) 582, 198 (2020).
- [24] U. Zondiner, A. Rozen, D. Rodan-Legrain, Y. Cao, R. Queiroz, T. Taniguchi, K. Watanabe, Y. Oreg, F. von Oppen, A. Stern

- *et al.*, Cascade of phase transitions and dirac revivals in magicangle graphene, Nature (London) **582**, 203 (2020).
- [25] A. L. Sharpe, E. J. Fox, A. W. Barnard, J. Finney, K. Watanabe, T. Taniguchi, M. A. Kastner, and D. Goldhaber-Gordon, Emergent ferromagnetism near threequarters filling in twisted bilayer graphene, Science 365, 605 (2019).
- [26] M. Serlin, C. L. Tschirhart, H. Polshyn, Y. Zhang, J. Zhu, K. Watanabe, T. Taniguchi, L. Balents, and A. F. Young, Intrinsic quantized anomalous Hall effect in a moiré heterostructure, Science 367, 900 (2019).
- [27] N. Bultinck, S. Chatterjee, and M. P. Zaletel, Mechanism for Anomalous Hall Ferromagnetism in Twisted Bilayer Graphene, Phys. Rev. Lett. 124, 166601 (2020).
- [28] Y. Saito, J. Ge, K. Watanabe, T. Taniguchi, E. Berg, and A. F. Young, Isospin Pomeranchuk effect and the entropy of collective excitations in twisted bilayer graphene, Nature 592, 220 (2021).
- [29] J. Kang and O. Vafek, Non-Abelian Dirac node braiding and near-degeneracy of correlated phases at odd integer filling in magic-angle twisted bilayer graphene, Phys. Rev. B 102, 035161 (2020).
- [30] T. Soejima, D. E. Parker, N. Bultinck, J. Hauschild, and M. P. Zaletel, Efficient simulation of moiré materials using the density matrix renormalization group, Phys. Rev. B 102, 205111 (2020).
- [31] Y. Cao, D. Chowdhury, D. Rodan-Legrain, O. Rubies-Bigorda, K. Watanabe, T. Taniguchi, T. Senthil, and P. Jarillo-Herrero, Strange Metal in Magic-Angle Graphene with Near Planckian Dissipation, Phys. Rev. Lett. 124, 076801 (2020).
- [32] Y. H. Kwan, G. Wagner, N. Chakraborty, S. H. Simon, and S. A. Parameswaran, Orbital Chern insulator domain walls and chiral modes in twisted bilayer graphene, arXiv:2007.07903 (2020).
- [33] Y. Cao, V. Fatemi, S. Fang, K. Watanabe, T. Taniguchi, E. Kaxiras, and P. Jarillo-Herrero, Unconventional superconductivity in magic-angle graphene superlattices, Nature (London) 556, 43 (2018).
- [34] X. Lu, P. Stepanov, W. Yang, M. Xie, M. A. Aamir, I. Das, C. Urgell, K. Watanabe, T. Taniguchi, G. Zhang et al., Superconductors, orbital magnets and correlated states in magic-angle bilayer graphene, Nature (London) 574, 653 (2019).
- [35] M. Yankowitz, S. Chen, H. Polshyn, Y. Zhang, K. Watanabe, T. Taniguchi, D. Graf, A. F. Young, and C. R. Dean, Tuning superconductivity in twisted bilayer graphene, Science 363, 1059 (2019).
- [36] F. Wu, A. H. MacDonald, and I. Martin, Theory of Phonon-Mediated Superconductivity in Twisted Bilayer Graphene, Phys. Rev. Lett. 121, 257001 (2018).
- [37] C. Xu and L. Balents, Topological Superconductivity in Twisted Multilayer Graphene, Phys. Rev. Lett. 121, 087001 (2018).
- [38] C.-C. Liu, L.-D. Zhang, W.-Q. Chen, and F. Yang, Chiral Spin Density Wave and d + id Superconductivity in the Magic-Angle-Twisted Bilayer Graphene, Phys. Rev. Lett. **121**, 217001 (2018).
- [39] H. Isobe, N. F. Q. Yuan, and L. Fu, Unconventional Superconductivity and Density Waves in Twisted Bilayer Graphene, Phys. Rev. X 8, 041041 (2018).

- [40] F. Guinea and N. R. Walet, Electrostatic effects, band distortions, and superconductivity in twisted graphene bilayers, Proc. Natl. Acad. Sci. USA 115, 13174 (2018).
- [41] J. Gonzalez and T. Stauber, Kohn-Luttinger Superconductivity in Twisted Bilayer Graphene, Phys. Rev. Lett. 122, 026801 (2019).
- [42] B. Lian, Z. Wang, and B. A. Bernevig, Twisted Bilayer Graphene: A Phonon-Driven Superconductor, Phys. Rev. Lett. 122, 257002 (2019).
- [43] Y.-Z. You and A. Vishwanath, Superconductivity from valley fluctuations and approximate SO(4) symmetry in a weak coupling theory of twisted bilayer graphene, npj Quantum Mater. **4**, 16 (2019).
- [44] F. Xie, Z. Song, B. Lian, and B. A. Bernevig, Topology-Bounded Superfluid Weight in Twisted Bilayer Graphene, Phys. Rev. Lett. **124**, 167002 (2020).
- [45] Y. Saito, J. Ge, K. Watanabe, T. Taniguchi, and A. F. Young, Independent superconductors and correlated insulators in twisted bilayer graphene, Nat. Phys. 16, 926 (2020).
- [46] P. Stepanov, I. Das, X. Lu, A. Fahimniya, K. Watanabe, T. Taniguchi, F. H. L. Koppens, J. Lischner, L. Levitov, and D. K. Efetov, Untying the insulating and superconducting orders in magic-angle graphene, Nature (London) 583, 375 (2020).
- [47] H. S. Arora, R. Polski, Y. Zhang, A. Thomson, Y. Choi, H. Kim, Z. Lin, I. Z. Wilson, X. Xu, J.-H. Chu *et al.*, Superconductivity in metallic twisted bilayer graphene stabilized by WSe₂, Nature (London) 583, 379 (2020).
- [48] E. Khalaf, S. Chatterjee, N. Bultinck, M. P. Zaletel, and A. Vishwanath, Charged skyrmions and topological origin of superconductivity in magic angle graphene, arXiv:2004.00638 (2020).
- [49] F. Wu and S. Das Sarma, Collective Excitations of Quantum Anomalous Hall Ferromagnets in Twisted Bilayer Graphene, Phys. Rev. Lett. **124**, 046403 (2020).
- [50] A. Julku, T. J. Peltonen, L. Liang, T. T. Heikkilä, and P. Törmä, Superfluid weight and Berezinskii-Kosterlitz-Thouless transition temperature of twisted bilayer graphene, Phys. Rev. B 101, 060505(R) (2020).
- [51] E. J. König, P. Coleman, and A. M. Tsvelik, Spin magnetometry as a probe of stripe superconductivity in twisted bilayer graphene, Phys. Rev. B **102**, 104514 (2020).
- [52] J. Kang and O. Vafek, Symmetry, Maximally Localized Wannier States, and a Low-Energy Model for Twisted Bilayer Graphene Narrow Bands, Phys. Rev. X 8, 031088 (2018).
- [53] M. Koshino, N. F. Q. Yuan, T. Koretsune, M. Ochi, K. Kuroki, and L. Fu, Maximally Localized Wannier Orbitals and the Extended Hubbard Model for Twisted Bilayer Graphene, Phys. Rev. X 8, 031087 (2018).
- [54] J. Ahn, S. Park, and B.-J. Yang, Failure of Nielsen-Ninomiya Theorem and Fragile Topology in Two-Dimensional Systems with Space-Time Inversion Symmetry: Application to Twisted Bilayer Graphene at Magic Angle, Phys. Rev. X 9, 021013 (2019).
- [55] H. C. Po, L. Zou, T. Senthil, and A. Vishwanath, Faithful tightbinding models and fragile topology of magic-angle bilayer graphene, Phys. Rev. B 99, 195455 (2019).
- [56] Z. Song, Z. Wang, W. Shi, G. Li, C. Fang, and B. A. Bernevig, All Magic Angles in Twisted Bilayer Graphene are Topological, Phys. Rev. Lett. 123, 036401 (2019).

- [57] J. Liu, J. Liu, and X. Dai, Pseudo landau level representation of twisted bilayer graphene: Band topology and implications on the correlated insulating phase, Phys. Rev. B **99**, 155415 (2019).
- [58] G. Tarnopolsky, A. J. Kruchkov, and A. Vishwanath, Origin of Magic Angles in Twisted Bilayer Graphene, Phys. Rev. Lett. 122, 106405 (2019).
- [59] Y. Fu, E. J. König, J. H. Wilson, Y.-Z. Chou, and J. H. Pixley, Magic-angle semimetals, npj Quantum Mater. 5, 71 (2020).
- [60] Y.-H. Zhang, D. Mao, Y. Cao, P. Jarillo-Herrero, and T. Senthil, Nearly flat Chern bands in moiré superlattices, Phys. Rev. B 99, 075127 (2019).
- [61] B. Lian, F. Xie, and B. A. Bernevig, Landau level of fragile topology, Phys. Rev. B 102, 041402(R) (2020).
- [62] X. Lu, B. Lian, G. Chaudhary, B. A. Piot, G. Romagnoli, K. Watanabe, T. Taniguchi, M. Poggio, A. H. MacDonald, B. A. Bernevig, and D. K. Efetov, Fingerprints of fragile topology in the Hofstadter spectrum of twisted bilayer graphene close to the second magic angle, arXiv:2006.13963 (2020).
- [63] B. Padhi, A. Tiwari, T. Neupert, and S. Ryu, Transport across twist angle domains in moiré graphene, Phys. Rev. Research 2, 033458 (2020).
- [64] J. Herzog-Arbeitman, Z.-D. Song, N. Regnault, and B. A. Bernevig, Hofstadter Topology: Noncrystalline Topological Materials at High Flux, Phys. Rev. Lett. 125, 236804 (2020).
- [65] J. H. Wilson, Y. Fu, S. Das Sarma, and J. H. Pixley, Disorder in twisted bilayer graphene, Phys. Rev. Research 2, 023325 (2020).
- [66] X. Liu, Z. Wang, K. Watanabe, T. Taniguchi, O. Vafek, and J. I. A. Li, Tuning electron correlation in magic-angle twisted bilayer graphene using coulomb screening, Science 371, 1261 (2021).
- [67] A. Kerelsky, L. J. McGilly, D. M. Kennes, L. Xian, M. Yankowitz, S. Chen, K. Watanabe, T. Taniguchi, J. Hone, C. Dean *et al.*, Maximized electron interactions at the magic angle in twisted bilayer graphene, Nature (London) 572, 95 (2019).
- [68] Y. Choi, H. Kim, Y. Peng, A. Thomson, C. Lewandowski, R. Polski, Y. Zhang, H. S. Arora, K. Watanabe, T. Taniguchi, J. Alicea, and S. Nadj-Perge, Tracing out correlated Chern insulators in magic angle twisted bilayer graphene, arXiv:2008.11746 (2020).
- [69] J. M. Park, Y. Cao, K. Watanabe, T. Taniguchi, and P. Jarillo-Herrero, Flavour Hund's coupling, correlated Chern gaps, and diffusivity in moiré flat bands, Nature 592, 43 (2021).
- [70] A. Rozen, J. M. Park, U. Zondiner, Y. Cao, D. Rodan-Legrain, T. Taniguchi, K. Watanabe, Y. Oreg, A. Stern, E. Berg, P. Jarillo-Herrero, and S. Ilani, Entropic evidence for a Pomeranchuk effect in magic angle graphene, Nature 592, 214 (2021).
- [71] G. W. Burg, J. Zhu, T. Taniguchi, K. Watanabe, A. H. MacDonald, and E. Tutuc, Correlated Insulating States in Twisted Double Bilayer Graphene, Phys. Rev. Lett. 123, 197702 (2019).
- [72] C. Shen, Y. Chu, Q. Wu, N. Li, S. Wang, Y. Zhao, J. Tang, J. Liu, J. Tian, K. Watanabe, T. Taniguchi, R. Yang, Z. Y. Meng, D. Shi, O. V. Yazyev, and G. Zhang, Correlated states in twisted double bilayer graphene, Nat. Phys. 16, 520 (2020).
- [73] Y. Cao, D. Rodan-Legrain, O. Rubies-Bigorda, J. M. Park, K. Watanabe, T. Taniguchi, and P. Jarillo-Herrero, Tunable

- correlated states and spin-polarized phases in twisted bilayer-bilayer graphene, Nature (London) **583**, 215 (2020).
- [74] X. Liu, Z. Hao, E. Khalaf, J. Yeon Lee, Y. Ronen, H. Yoo, D. H. Najafabadi, K. Watanabe, T. Taniguchi, A. Vishwanath, and P. Kim, Tunable spin-polarized correlated states in twisted double bilayer graphene, Nature 583, 221 (2020).
- [75] G. Chen, L. Jiang, S. Wu, B. Lyu, H. Li, B. L. Chittari, K. Watanabe, T. Taniguchi, Z. Shi, J. Jung, Y. Zhang, and F. Wang, Evidence of a gate-tunable Mott insulator in a trilayer graphene moiré superlattice, Nat. Phys. 15, 237 (2019).
- [76] G. Chen, A. L. Sharpe, P. Gallagher, I. T. Rosen, E. J. Fox, L. Jiang, B. Lyu, H. Li, K. Watanabe, T. Taniguchi, J. Jung, Z. Shi, D. Goldhaber-Gordon, Y. Zhang, and F. Wang, Signatures of tunable superconductivity in a trilayer graphene moiré superlattice, Nature (London) 572, 215 (2019).
- [77] G. Chen, A. L. Sharpe, E. J. Fox, Y.-H. Zhang, S. Wang, L. Jiang, B. Lyu, H. Li, K. Watanabe, T. Taniguchi, Z. Shi, T. Senthil, D. Goldhaber-Gordon, Y. Zhang, and F. Wang, Tunable correlated Chern insulator and ferromagnetism in a moiré superlattice, Nature (London) 579, 56 (2020).
- [78] G. W. Burg, B. Lian, T. Taniguchi, K. Watanabe, B. A. Bernevig, and E. Tutuc, Evidence of emergent symmetry and valley Chern number in twisted double-bilayer graphene, arXiv:2006.14000 (2020).
- [79] L. Zou, H. C. Po, A. Vishwanath, and T. Senthil, Band structure of twisted bilayer graphene: Emergent symmetries, commensurate approximants, and Wannier obstructions, Phys. Rev. B 98, 085435 (2018).
- [80] A. Bouhon, A. M. Black-Schaffer, and R.-J. Slager, Wilson loop approach to fragile topology of split elementary band representations and topological crystalline insulators with time-reversal symmetry, Phys. Rev. B 100, 195135 (2019).
- [81] K. Hejazi, C. Liu, H. Shapourian, X. Chen, and L. Balents, Multiple topological transitions in twisted bilayer graphene near the first magic angle, Phys. Rev. B 99, 035111 (2019).
- [82] K. Hejazi, C. Liu, and L. Balents, Landau levels in twisted bilayer graphene and semiclassical orbits, Phys. Rev. B 100, 035115 (2019).
- [83] X.-C. Wu, C.-M. Jian, and C. Xu, Coupled-wire description of the correlated physics in twisted bilayer graphene, Phys. Rev. B 99, 161405(R) (2019).
- [84] A. Thomson, S. Chatterjee, S. Sachdev, and M. S. Scheurer, Triangular antiferromagnetism on the honeycomb lattice of twisted bilayer graphene, Phys. Rev. B **98**, 075109 (2018).
- [85] K. Seo, V. N. Kotov, and B. Uchoa, Ferromagnetic Mott State in Twisted Graphene Bilayers at the Magic Angle, Phys. Rev. Lett. 122, 246402 (2019).
- [86] K. Hejazi, X. Chen, and L. Balents, Hybrid Wannier Chern bands in magic angle twisted bilayer graphene and the quantized anomalous Hall effect, Phys. Rev. Research 3, 013242 (2021).
- [87] X. Hu, T. Hyart, D. I. Pikulin, and E. Rossi, Geometric and Conventional Contribution to the Superfluid Weight in Twisted Bilayer Graphene, Phys. Rev. Lett. 123, 237002 (2019).
- [88] M. Christos, S. Sachdev, and M. Scheurer, Superconductivity, correlated insulators, and Wess-Zumino-Witten terms in twisted bilayer graphene, PNAS 117, 29543 (2020).
- [89] C. Lewandowski, D. Chowdhury, and J. Ruhman, Pairing in magic-angle twisted bilayer graphene: role of phonon and plasmon umklapp, arXiv:2007.15002 (2020).

- [90] J. Liu and X. Dai, Theories for the correlated insulating states and quantum anomalous Hall phenomena in twisted bilayer graphene, Phys. Rev. B **103**, 035427 (2021).
- [91] T. Cea and F. Guinea, Band structure and insulating states driven by coulomb interaction in twisted bilayer graphene, Phys. Rev. B **102**, 045107 (2020).
- [92] Y. Zhang, K. Jiang, Z. Wang, and F. Zhang, Correlated insulating phases of twisted bilayer graphene at commensurate filling fractions: A Hartree-Fock study, Phys. Rev. B 102, 035136 (2020).
- [93] S. Liu, E. Khalaf, J. Y. Lee, and A. Vishwanath, Nematic topological semimetal and insulator in magic-angle bilayer graphene at charge neutrality, Phys. Rev. Research 3, 013033 (2021).
- [94] Y. Da Liao, Z. Y. Meng, and X. Y. Xu, Valence Bond Orders at Charge Neutrality in a Possible Two-Orbital Extended Hubbard Model for Twisted Bilayer Graphene, Phys. Rev. Lett. 123, 157601 (2019).
- [95] Y. D. Liao, J. Kang, C. N. Breiø, X. Y. Xu, H.-Q. Wu, B. M. Andersen, R. M. Fernandes, and Z. Y. Meng, Correlation-Induced Insulating Topological Phases at Charge Neutrality in Twisted Bilayer Graphene, Phys. Rev. X 11, 011014 (2021).
- [96] L. Classen, C. Honerkamp, and M. M. Scherer, Competing phases of interacting electrons on triangular lattices in moiré heterostructures, Phys. Rev. B 99, 195120 (2019).
- [97] D. M. Kennes, J. Lischner, and C. Karrasch, Strong correlations and d + id superconductivity in twisted bilayer graphene, Phys. Rev. B **98**, 241407(R) (2018).
- [98] P. M. Eugenio and C. B. Dağ, DMRG study of strongly interacting \mathbb{Z}_2 flatbands: A toy model inspired by twisted bilayer graphene, SciPost Phys. Core 3, 015 (2020).
- [99] Y. Huang, P. Hosur, and H. K. Pal, Quasi-flat-band physics in a two-leg ladder model and its relation to magic-angle twisted bilayer graphene, Phys. Rev. B **102**, 155429 (2020).
- [100] T. Huang, L. Zhang, and T. Ma, Antiferromagnetically ordered Mott insulator and d + id superconductivity in twisted bilayer graphene: A quantum monte carlo study, Sci. Bull. **64**, 310 (2019).
- [101] H. Guo, X. Zhu, S. Feng, and R. T. Scalettar, Pairing symmetry of interacting fermions on a twisted bilayer graphene superlattice, Phys. Rev. B 97, 235453 (2018).
- [102] P. J. Ledwith, G. Tarnopolsky, E. Khalaf, and A. Vishwanath, Fractional Chern insulator states in twisted bilayer graphene: An analytical approach, Phys. Rev. Research 2, 023237 (2020).
- [103] C. Repellin, Z. Dong, Y.-H. Zhang, and T. Senthil, Ferromagnetism in Narrow Bands of Moiré Superlattices, Phys. Rev. Lett. 124, 187601 (2020).
- [104] A. Abouelkomsan, Z. Liu, and E. J. Bergholtz, Particle-Hole Duality, Emergent Fermi Liquids, and Fractional Chern Insulators in Moiré Flatbands, Phys. Rev. Lett. 124, 106803 (2020).
- [105] C. Repellin and T. Senthil, Chern bands of twisted bilayer graphene: Fractional Chern insulators and spin phase transition, Phys. Rev. Research 2, 023238 (2020).
- [106] O. Vafek and J. Kang, Renormalization Group Study of Hidden Symmetry in Twisted Bilayer Graphene with Coulomb Interactions, Phys. Rev. Lett. 125, 257602 (2020).

- [107] R. M. Fernandes and J. W. F. Venderbos, Nematicity with a twist: Rotational symmetry breaking in a moiré superlattice, Sci. Adv. 6, eaba8834 (2020).
- [108] J. Wang, Y. Zheng, A. J. Millis, and J. Cano, Chiral approximation to twisted bilayer graphene: Exact intra-valley inversion symmetry, nodal structure and implications for higher magic angles, arXiv:2010.03589 (2020).
- [109] B. A. Bernevig, Z.-D. Song, N. Regnault, and B. Lian, Twisted bilayer graphene. I. Matrix elements, approximations, perturbation theory, and a $k \cdot p$ two-band model, Phys. Rev. B **103**, 205411 (2021).
- [110] B. A. Bernevig, Z.-D. Song, N. Regnault, and B. Lian, Twisted bilayer graphene. III. Interacting Hamiltonian and exact symmetries, Phys. Rev. B 103, 205413 (2021).
- [111] B. Lian, Z.-D. Song, N. Regnault, D. K. Efetov, A. Yazdani, and B. A. Bernevig, Twisted bilayer graphene. IV. Exact insulator ground states and phase diagram, Phys. Rev. B 103, 205414 (2021).
- [112] B. A. Bernevig, B. Lian, A. Cowsik, F. Xie, N. Regnault, and Z.-D. Song, Twisted bilayer graphene. V. Exact analytic many-body excitations in Coulomb Hamiltonians: Charge gap, Goldstone modes, and absence of Cooper pairing, Phys. Rev. B 103, 205415 (2021).
- [113] F. Xie, A. Cowsik, Z.-D. Song, B. Lian, B. A. Bernevig, and N. Regnault, Twisted bilayer graphene. VI. An exact diagonalization study at nonzero integer filling, Phys. Rev. B 103, 205416 (2021).
- [114] H. C. Po, H. Watanabe, and A. Vishwanath, Fragile Topology and Wannier Obstructions, Phys. Rev. Lett. **121**, 126402 (2018).
- [115] J. Cano, B. Bradlyn, Z. Wang, L. Elcoro, M. G. Vergniory, C. Felser, M. I. Aroyo, and B. A. Bernevig, Topology of Disconnected Elementary Band Representations, Phys. Rev. Lett. 120, 266401 (2018).
- [116] D. V. Else, H. C. Po, and H. Watanabe, Fragile topological phases in interacting systems, Phys. Rev. B 99, 125122 (2019)
- [117] J. L. Mañes, Fragile phonon topology on the honeycomb lattice with time-reversal symmetry, Phys. Rev. B 102, 024307 (2020).
- [118] A. Alexandradinata, J. Höller, C. Wang, H. Cheng, and L. Lu, Crystallographic splitting theorem for band representations and fragile topological photonic crystals, Phys. Rev. B **102**, 115117 (2020).
- [119] K. Uchida, S. Furuya, J.-I. Iwata, and A. Oshiyama, Atomic corrugation and electron localization due to moiré patterns in twisted bilayer graphenes, Phys. Rev. B **90**, 155451 (2014).
- [120] M. M. van Wijk, A. Schuring, M. I. Katsnelson, and A. Fasolino, Relaxation of moiré patterns for slightly misaligned identical lattices: Graphene on graphite, 2D Mater. 2, 034010 (2015).
- [121] S. Dai, Y. Xiang, and D. J. Srolovitz, Twisted bilayer graphene: Moiré with a twist, Nano Lett. 16, 5923 (2016).
- [122] S. K. Jain, V. Juričić, and G. T. Barkema, Structure of twisted and buckled bilayer graphene, 2D Mater. 4, 015018 (2016).
- [123] S. V. Gallego, E. S. Tasci, G. Flor, J. M. Perez-Mato, and M. I. Aroyo, Magnetic symmetry in the Bilbao crystallographic server: A computer program to provide systematic absences of magnetic neutron diffraction, J. Appl. Crystallogr. 45, 1236 (2012).

- [124] A. Alexandradinata, Z. Wang, and B. A. Bernevig, Topological Insulators from Group Cohomology, Phys. Rev. X 6, 021008 (2016).
- [125] Z. Wang, A. Alexandradinata, R. J. Cava, and B. A. Bernevig, Hourglass fermions, Nature (London) 532, 189 (2016).
- [126] R. Yu, X. L. Qi, A. Bernevig, Z. Fang, and X. Dai, Equivalent expression of \mathbb{Z}_2 topological invariant for band insulators using the non-Abelian Berry connection, Phys. Rev. B **84**, 075119 (2011).
- [127] A. Alexandradinata, X. Dai, and B. A. Bernevig, Wilson-loop characterization of inversion-symmetric topological insulators, Phys. Rev. B 89, 155114 (2014).
- [128] L. Fu and C. L. Kane, Time reversal polarization and a Z_2 adiabatic spin pump, Phys. Rev. B **74**, 195312 (2006).
- [129] T. Fukui and Y. Hatsugai, Quantum spin Hall effect in three dimensional materials: Lattice computation of z_2 topological invariants and its application to Bi and Sb, J. Phys. Soc. Jpn. **76**, 053702 (2007).
- [130] B. A. Bernevig and T. L. Hughes, *Topological Insulators and Topological Superconductors* (Princeton University, Princeton, NJ, 2013).
- [131] J. Ahn, D. Kim, Y. Kim, and B.-J. Yang, Band Topology and Linking Structure of Nodal Line Semimetals with \mathbb{Z}_2 Monopole Charges, Phys. Rev. Lett. **121**, 106403 (2018).
- [132] F. N. Ünal, A. Bouhon, and R.-J. Slager, Topological Euler Class as a Dynamical Observable

- in Optical Lattices, Phys. Rev. Lett. **125**, 053601 (2020).
- [133] Q. Wu, A. A Soluyanov, and T. Bzdušek, Non-Abelian band topology in noninteracting metals, Science 365, 1273 (2019).
- [134] C. Mora, N. Regnault, and B. A. Bernevig, Flatbands and Perfect Metal in Trilayer Moiré Graphene, Phys. Rev. Lett. 123, 026402 (2019).
- [135] C. Fang, M. J. Gilbert, and B. A. Bernevig, Bulk topological invariants in noninteracting point group symmetric insulators, Phys. Rev. B 86, 115112 (2012).
- [136] T. L. Hughes, E. Prodan, and B. A. Bernevig, Inversionsymmetric topological insulators, Phys. Rev. B 83, 245132 (2011).
- [137] A. M. Turner, Y. Zhang, R. S. K. Mong, and A. Vishwanath, Quantized response and topology of magnetic insulators with inversion symmetry, Phys. Rev. B 85, 165120 (2012).
- [138] N. N. T. Nam and M. Koshino, Lattice relaxation and energy band modulation in twisted bilayer graphene, Phys. Rev. B 96, 075311 (2017).
- [139] M. Koshino and N. N. T. Nam, Effective continuum model for relaxed twisted bilayer graphene and moiré electron-phonon interaction, Phys. Rev. B 101, 195425 (2020).
- [140] S. Fang, S. Carr, Z. Zhu, D. Massatt, and E. Kaxiras, Angle-dependent ab-initio low-energy Hamiltonians for a relaxed twisted bilayer graphene heterostructure, arXiv:1908.00058 (2019).